Article

# The CCL2-CCR2 axis drives neuromuscular denervation in amyotrophic lateral sclerosis

Bernát Nógrádi [1,2,3,4], Kinga Molnár[4], Rebeka Kristóf[4], Orsolya Horváth[3], Yu-Ting Huang[1,2], Zara Ridgway [1,2], Amaia Elicegui [5,6], Sandra Fuertes-Alvarez[5], Sonia Alonso-Martin [5,6], Gábor J. Szebeni[7], Nikolett Gémes[7], Abdullah Ramadan[1,2,8], Hannah L. Smith [1,2], István A. Krizbai[4,9], Roland Patai[4], László Siklós[4], Péter Klivényi [3,10], Helena Chaytow [1,2,11] & Thomas H. Gillingwater [1,2,11] ✉

Systemic immune changes have been implicated in amyotrophic lateral sclerosis (ALS), but precise mechanisms and cellular targets remain unknown. Neuromuscular junction (NMJ) denervation is another major pathophysiological event in ALS, but it remains unclear whether immune system dysregulation contributes to this process. Here, we report leukocyte and macrophage infiltration in ALS patient-derived skeletal muscle biopsies. Immune cell infiltration was replicated across the hTDP-43, TDP-43[A315T] (male only) and TDP-43[M337V] mouse models, occurring from pre-symptomatic stages and targeted to NMJ-enriched muscle regions. Proteomic analysis implicated the CCL2-CCR2 axis as a driving factor. CCL2^{+} cells were enriched around NMJs in hTDP-43 mice, and in ALS patient skeletal muscle. Local treatment with CCL2-neutralising antibodies or normal IgG antibodies in hTDP-43 mice reduced leukocyte infiltration and ameliorated NMJ denervation. These results demonstrate that the CCL2-CCR2 axis drives immune cell infiltration targeting NMJs in ALS, identifying a potential avenue for therapeutic intervention to prevent NMJ denervation.

Amyotrophic lateral sclerosis (ALS) is a fatal neurodegenerative disorder, characterised by the progressive loss of upper and lower motor neurons. Alongside motor neuron degeneration, denervation of the neuromuscular junction (NMJ) is a major pathological hallmark of ALS, leading to muscle weakness and atrophy, the primary clinical manifestation of the disease[1]. Whilst the exact cellular location of disease onset remains unclear[2], there is compelling evidence that NMJ denervation is an early event that precedes motor unit loss[3–5].

The pathophysiological changes that lead to motor neuron death are considered to be multifaceted[6]. However, one of the core components contributing to neurodegeneration is activation and dysregulation of the immune system[7]. These immune-related alterations emerge both in the central nervous system (CNS) (i.e.

[1]Edinburgh Medical School: Biomedical Sciences, University of Edinburgh, Edinburgh, UK. [2]Euan MacDonald Centre for Motor Neuron Disease Research, Edinburgh, UK. [3]Department of Neurology, Albert Szent-Györgyi Health Centre, University of Szeged, Szeged, Hungary. [4]Department of Biophysics, HUN-REN Biological Research Centre, Szeged, Hungary. [5]Stem Cells and Aging Group, Biogipuzkoa Health Research Institute, San Sebastian, Spain. [6]CIBERNED, ISCIII (CIBER, Carlos III Institute, Spanish Ministry of Sciences and Innovation), Madrid, Spain. [7]Laboratory of Functional Genomics, Core Facility, HUN-REN Biological Research Centre, Szeged, Hungary. [8]College of Sciences and Health Professions, King Saud bin Abdulaziz for Health Sciences, Jeddah, Saudi Arabia. [9]Institute of Life Sciences, Vasile Goldiş Western University of Arad, Arad, Romania. [10]HUN-REN-SZTE Neuroscience Research Group, Hungarian Research Network, University of Szeged, Szeged, Hungary. [11]These authors contributed equally: Helena Chaytow, Thomas H. Gillingwater. ✉e-mail: t.gillingwater@ed.ac.uk

1

neuroinflammation) and as systemic alterations[8]. Immune dysregulation in ALS displays features of autoimmunity, excessive inflammation and an inefficient immune response, meaning that non-selective systemic immunosuppressive therapies are too simplistic an approach to be effective[9]. Currently, the best-characterised systemic inflammatory alteration is an elevation of pro-inflammatory cytokines and chemokines in the blood serum of ALS patients, including tumor necrosis factor alpha (TNF-α), interleukin-6 (IL-6) and chemokine (C-C motif) ligand 2 (CCL2)[10–12]. These inflammatory proteins are considered to be potent chemoattractants, capable of inducing robust immune cell recruitment through receptor-mediated pathways, such as the CCL2-driven activation of the C-C chemokine receptor type 2 (CCR2)[13]. Immune cell changes have also been reported in the blood of ALS patients, such as increased neutrophil granulocyte numbers[14] and a decrease in regulatory T-cells ($T_{reg}$)[15], while $T_{reg}$ cells were also dysfunctional[16]. Interestingly, some clinical studies reported an increase in the number of cluster of differentiation (CD)4+ T-helper cells[17], while others showed a reduced number[18], highlighting the heterogeneity of inflammatory processes in ALS. Some of these systemic immune markers were also shown to correlate with clinical parameters: plasma IL-10 and TNF-α negatively correlated with survival[12], leukocyte and CD4+ cell count positively correlated with disease progression[14], while $T_{reg}$ dysfunction negatively correlated with disease burden and the rate of progression[16].

Whilst these findings indicate a prominent role for systemic immune processes, the underlying pathomechanisms that link such immune processes to motor neuron degeneration remain largely unknown. As the major contact point between the CNS and the periphery, the neuromuscular system may represent a crucial link between these two elements of disease pathogenesis. Indeed, evidence suggests that immune cells may directly interact with neural components of the muscle tissue in ALS models[19,20]. Therefore, we reasoned that immune responses occurring locally within skeletal muscle might actively contribute to NMJ denervation and disease progression. Here, we report increased immune cell infiltration in muscle samples of ALS patients. We report that these phenotypes can be recapitulated in three different ALS mouse models, regardless of age of onset or speed of disease progression, and we identify the CCL2-CCR2 axis as a driver of immune cell infiltration. Finally, we demonstrate that targeted immunomodulatory treatment can ameliorate NMJ denervation, revealing a potential therapeutic approach for ALS.

## Results
### Infiltration of immune cells in ALS patient muscle and mouse models
To characterise the effect of the immune system alterations on skeletal muscle in ALS, we obtained muscle samples from ALS patients to compare with healthy controls (Table 1). Compared to the relatively low number of resident leukocytes in muscle samples from control individuals, we observed a marked elevation of immune cells in ALS patient muscles (Fig. 1A) with quantification of CD45+ cells revealing a significant increase in ALS muscle samples (26.60 vs. 84.23 cells/mm², $p = 0.0009$; Fig. 1B). Using CD68+ as a marker for monocytes and macrophages, we showed significant infiltration of these immune cell subtypes in ALS patients (8.95 vs. 26.07 cells/mm², $p = 0.0388$; Fig. 1C, D). Using a co-label of either dystrophin (Fig. 1B) or laminin (Fig. 1D, Supplementary Fig. 1A), we observed notable changes in the skeletal muscle architecture, confirming neuromuscular pathology. Due to the challenges in obtaining patient muscle samples, the samples analysed here are from a range of different muscles (Table 1). However, if analysed separately, there does not seem to be a difference in infiltration between muscle types (Supplementary Fig. 1B, C). These experiments confirm that immune cell infiltration is a feature of muscle pathology in ALS patients.

Muscle biopsy samples from patients are limited due to restricted accessibility and come with obvious limitations with regards to experimental intervention. In addition, biopsies are sampled at random along the muscle fibre, meaning that the chances of sampling from the innervation band in any given biopsy are slim. Therefore, in order to examine interactions between immune cell infiltration and NMJ denervation (an early driver of neuromuscular pathology in ALS)[21], we first confirmed whether immune cell infiltration into skeletal muscle was recapitulated in mouse models of ALS. There is no ideal mouse model that replicates all features of ALS precisely, partly due to the huge heterogeneity amongst patients. We therefore investigated immune cell infiltration in the skeletal muscle of three independent mouse models: a fast-progressing, early-onset model (hTDP43$^{Tg/Tg}$)[22], a fast-progressing adult-onset model (TDP-43$^{A315T}$)[23] and a slow-progressing, late-onset model (TDP-43$^{M337V}$)[24]. At time points with previously described denervation, all three models showed significant immune cell infiltration (Fig. 2). Compared to the modest number of resident immune cells present in wild-type (WT) control mice at postnatal day 19 (P19), CD45+ leukocyte numbers were 2.18 times higher in the innervation zone of the highly vulnerable *gastrocnemius* (GC) muscle of late symptomatic (P19) hTDP-43$^{Tg/Tg}$ mice (97.13 vs. 211.6 cells/mm², $p = 0.0286$; Fig. 2A). The adult-onset, fast progressing TDP-43$^{A315T}$ model, at a late symptomatic time point (P90), also showed twice the number of immune cells in the innervation zone around the NMJs (81.03 vs 180.5 cells/mm², $p = 0.0004$; Fig. 2B). Finally, at an early symptomatic time point of the TDP-43$^{M337V}$ model (12 months), where the mice show only mild motor impairment and early stages of denervation[24], we still observed a significantly increased number of infiltrating leukocytes (105.60 vs 142.90 cells/mm², $p = 0.0427$; Fig. 2C). This analysis shows that the presence of leukocytes in the skeletal muscle is a consistent phenotype across human patients and ALS mouse models, regardless of age or speed of disease progression.

Since this feature of immune cell infiltration into skeletal muscle was clearly conserved across different murine models, mimicking our

**Table 1 | Patient information**

| Sample | Diagnosis | Disease onset | Genetics | Biopsy status | Muscle |
|--------|-----------|---------------|----------|---------------|--------|
| CTRL-1 | control | n/a | n/a | alive | *gluteus medius* |
| CTRL-2 | control | n/a | n/a | alive | *vastus lateralis* |
| CTRL-3 | control | n/a | n/a | alive | *quadriceps* |
| CTRL-4 | control | n/a | n/a | alive | *biceps* |
| ALS-1 | fALS | bulbar | *TBK1* c.701+1 G > A | *post mortem* | *tibialis anterior* |
| ALS-2 | sALS | spinal | unknown | alive | *tibialis anterior* |
| ALS-3 | fALS | spinal | unknown | *post mortem* | *quadriceps* |
| ALS-4 | fALS | spinal | *TARDBP* c.1055 A > G p.(Asn352Ser) | alive | *biceps* |

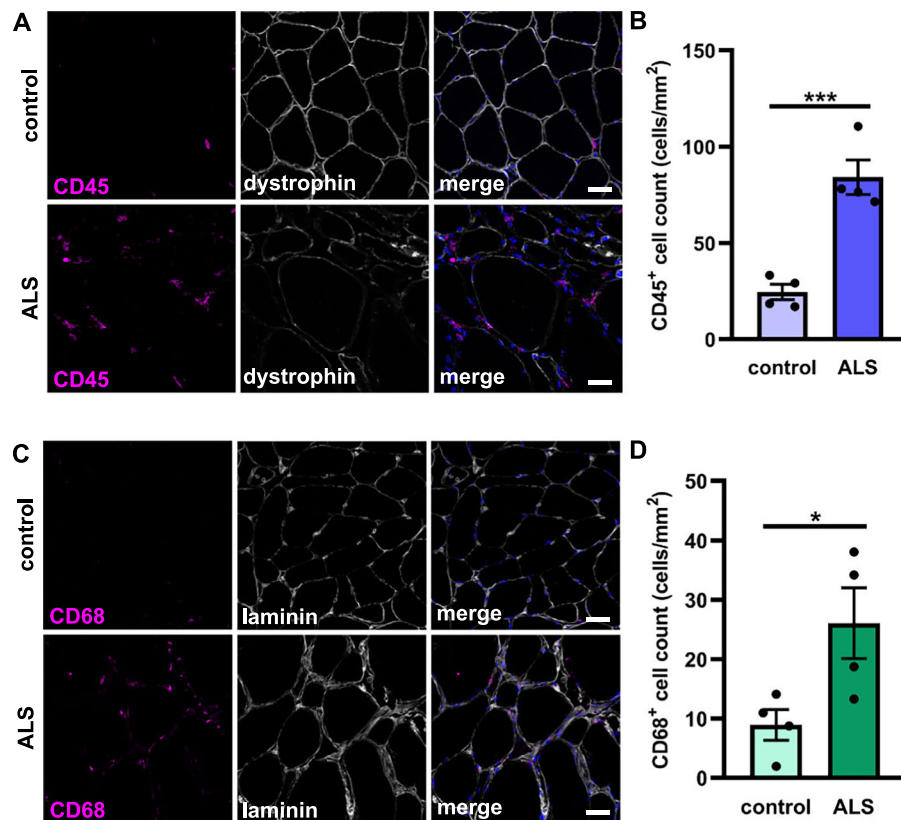*CTRL* control, *fALS* familial ALS, *sALS* sporadic ALS, *n/a* not applicable.

**Fig. 1 | Immune cell infiltration in skeletal muscle of ALS patients. A** CD45$^+$ leukocytes in skeletal muscle (cross section) of control individuals ("control") and ALS patients ("ALS"). Dystrophin co-staining also revealed notable changes in skeletal muscle architecture in ALS samples, confirming the presence of neuro-muscular pathology. Scale bar = 40 μm. **B** Quantification of CD45$^+$ cells in control ($n = 4$) and ALS ($n = 4$) patient samples. Each data point represents an average of 10 fields of view per patient. **C** CD68$^+$ macrophage cell count in skeletal muscle (cross section) of control individuals and ALS patients. Laminin co-staining also revealed notable changes in skeletal muscle architecture in ALS samples, confirming the presence of neuromuscular pathology. Scale bar = 40 μm. **D** Quantification of CD68$^+$ cells in control ($n = 4$) and ALS ($n = 4$) patient samples. Each data point represents an average of 10 fields of view per patient. Data is presented as mean ± sem. Both datasets were analysed using unpaired, two-tailed t-tests, (**B**) $p = 0.0009$, (**D**) $p = 0.0388$. * = $p < 0.05$; *** = $p < 0.001$.

findings in ALS patients, we sought to further characterise this pathological feature using hTDP-43$^{Tg/Tg}$ ALS mice. This model exhibits severe, progressive, hindlimb-dominant muscle weakness, and previous characterisation of NMJ pathology in these mice revealed distinctive vulnerability across different hindlimb muscles with respect to denervation[22]. In order to assess whether this distinctive pattern of neuromuscular pathology was associated with locally-controlled immune responses we initially compared the highly vulnerable GC muscle to the only modestly affected *tibialis anterior* (TA) and *extensor digitorum longus* (EDL) muscles (Supplementary Fig. 2A–C). There was no significant change in leukocyte number in the innervation zone of the less vulnerable TA and EDL muscles, although we observed a trend towards increased immune cell infiltration (TA: 89.95 vs. 142.6, $p = 0.1737$; EDL: 131.9 vs. 207.9 cells/mm$^2$, $p = 0.0964$; Supplementary Fig. 3A–C).

Subsequent quantification of CD68$^+$ macrophages confirmed elevated numbers of immune cells in muscles with increased neuromuscular vulnerability, as the GC muscle exhibited a robust 2.3-fold increase in the innervation zone (38.47 vs. 88.32 cells/mm$^2$, $p = 0.0034$; Fig. 3A, D), while macrophage counts remained unchanged in the TA and EDL muscles (TA: 49.63 vs. 41.05, $p = 0.8571$, Fig. 3B, E; EDL: 62.74 vs. 50.35 cells/mm$^2$, $p = 0.6816$; Fig. 3C, F). Evaluation of leukocyte and macrophage infiltration in the non-innervation zone, as defined by an absence of α-bungarotoxin (BTX)-labeled motor endplates, revealed a similar tendency: both CD45$^+$ and CD68$^+$ cell counts were increased in the GC muscle of late symptomatic hTDP-43$^{Tg/Tg}$ mice (CD45: 74.94 vs. 131.5, $p = 0.0201$; CD68: 28.5 vs. 64.35 cells/mm$^2$, $p = 0.0408$; Supplementary Fig. 3D, E), but no significant change was detected in the TA and EDL muscles (CD45 in TA: 96.3 vs. 86.72, $p = 0.7885$; CD45 in EDL: 124.1 vs. 150.2, $p = 0.3992$; CD68 in TA: 36.14 vs. 29.72, $p = 0.6710$; CD68 in EDL: 53.83 vs. 52.99 cells/mm$^2$, $p = 0.9746$; Supplementary Fig. 3D, E). Overall, we observed a greater degree of leukocyte infiltration at the innervation zone compared to other regions in the muscle.

Taken together, these results demonstrate that NMJ denervation correlates robustly with leukocyte and macrophage recruitment in skeletal muscle at late symptomatic disease stages, whilst in more modestly affected muscles, immune cell counts remained relatively unchanged. Thus, the hTDP-43$^{Tg/Tg}$ mouse model recapitulates the phenomenon of leukocyte infiltration observed in the affected muscles of ALS patients facilitating more detailed cellular and molecular characterisation.

It has previously been shown that motor neuron loss and NMJ denervation coincides with the appearance of the first clinical symptoms at around postnatal day 15 (P15) in hTDP-43$^{Tg/Tg}$ mice[22]. Thus, to assess whether the immune cell infiltration identified at late symptomatic stages preceded, or responded to, NMJ denervation we examined tissue from both P7 (presymptomatic) and P15 (early symptomatic) mice in the severely affected GC muscle. Due to the fast-progressive nature of this model, these time points coincide with the developmental maturation of the NMJ, during which immune processes play a role in synapse elimination[25]. Thus, we expected to
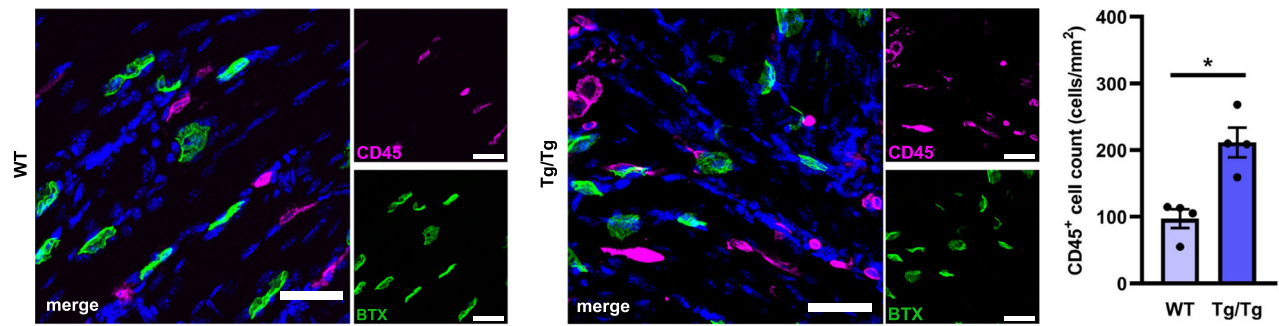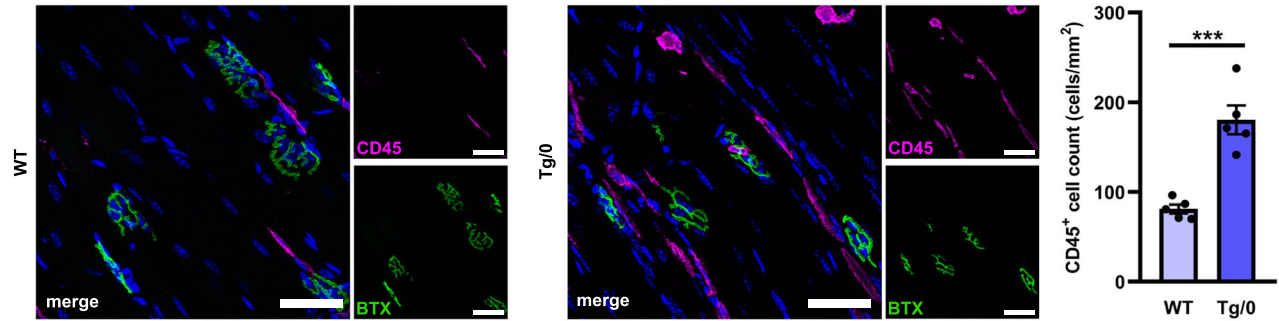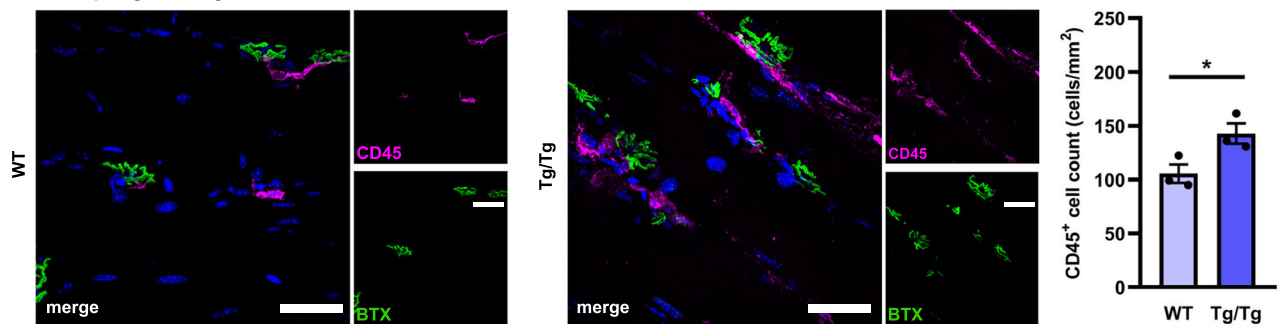
**Fig. 2 | Immune cell infiltration is a common feature across animal models of ALS. A** Immunohistochemical analysis of CD45^{+} cells infiltrating into the innervation zone (NMJs visualised with α-bungarotoxin, BTX) of *gastrocnemius* (GC) muscle from late-symptomatic (postnatal day 19) hTDP43[Tg/Tg] mice (Tg/Tg; $n = 4$) versus wild-type littermate controls (WT; $n = 4$). **B** Immunohistochemical analysis of CD45^{+} cells infiltrating into the innervation zone (NMJs visualised with α-bungar-otoxin, BTX) of GC muscle from late-symptomatic TDP-43[A315T] mice (postnatal day 90; Tg/0; $n = 5$) versus WT littermate controls ($n = 5$). **C** Immunohistochemical analysis of CD45^{+} cells infiltrating the innervation zone (NMJs visualised with α-bungarotoxin, BTX) of GC muscle from early-symptomatic TDP-43[M337V] mice (12 months old; Tg/Tg; $n = 3$) versus WT littermate controls ($n = 3$). Data points represent an average from 10 fields of view from 1 mouse. Data is presented as mean ± sem. Scale bars = 40 μm. Data analysis: (**A**) two-tailed Mann-Whitney test [Shapiro-Wilk normality test, WT group: $p = 0.0328$, Tg/Tg group: $p = 0.6879$], $p = 0.0286$, (**B**) unpaired, two-tailed t-test, $p = 0.0004$, (**C**) unpaired, two-tailed t-test, $p = 0.0427$. * = $p < 0.05$; *** = $p < 0.001$.

see a higher number of immune cells in skeletal muscle at early time points of WT littermates. Despite this, CD45 quantification revealed significantly increased leukocyte infiltration in the innervation zone of the GC muscle at both presymptomatic (264.2 vs 472.0 cells/mm², $p = 0.0003$; Fig. 4A, C) and early symptomatic (204.8 vs. 283.2 cells/mm², $p < 0.0001$; Fig. 4B, C) disease stages, above normal develop-mental levels. Replotting data from late-symptomatic disease stages (P19, Fig. 2) confirmed that while levels of immune cell infiltration fall with maturation in WT mice, hTDP-43[Tg/Tg] muscle continued to show significantly higher numbers of leukocytes. In the non-innervation zone of the GC muscle, the leukocyte count was slightly elevated during these earlier disease stages (P7: 256.9 vs 346.7 cells/mm², $p = 0.0297$; P15: 167.0 vs 228.8 cells/mm², $p = 0.0237$; Supplementary Fig. 4), but this increase was not as striking as in the innervation zone (P7 hTDP-43[Tg/Tg] IZ vs. NIZ: 346.7 vs 472.0 cells/mm², $p = 0.0206$; P15 hTDP-43[Tg/Tg] IZ vs. NIZ: 228.8 vs. 283.2 cells/mm², $p = 0.0217$,

unpaired, two-tailed t-test). This suggests that the earliest immune responses were focused primarily on the region of muscle where NMJs are located. Quantification of CD68^{+} macrophages showed no difference compared to the WT controls at P7 and P15 (Fig. 4D; Supplementary Fig. 4). When late-symptomatic time point data were replotted (P19, data from Fig. 3) we observed the same trend, where WT macrophage numbers continued to fall with maturation but macrophage numbers in hTDP-43[Tg/Tg] muscle became significantly higher. As the CD68-labeled macrophage population constitutes only a subset of total leukocytes, we concluded that the CD45-based quantification serves as a more reliable and robust approach for the detection of immune cell infiltration/proliferation in our analysis. Together, we demonstrated leukocyte infiltration in the innervation zone of pre- and early symptomatic GC muscles of hTDP-43[Tg/Tg] mice, compared to their age-matched WT control groups, indicating that the immune cell response precedes overt NMJ denervation.
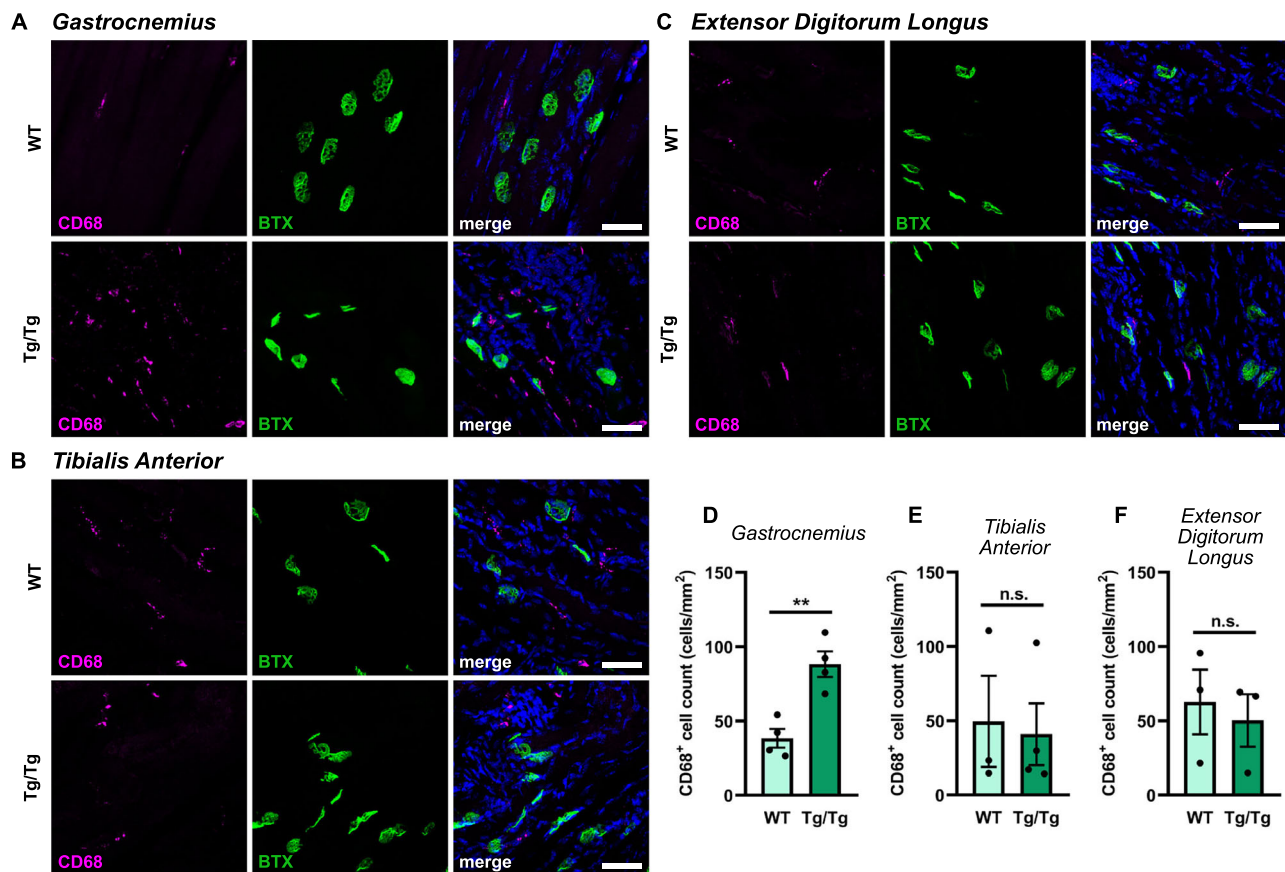
**Fig. 3 | Degree of macrophage infiltration correlates with vulnerability to NMJ denervation. A–C** Immunohistochemical analysis of CD68+ macrophages in the innervation zone of the *gastrocnemius* (GC; **A**), *tibialis anterior* (TA; **B**) and *extensor digitorum longus* (EDL; **C**) muscle (longitudinal section) of control wild-type (WT) and hTDP-43Tg/Tg mice (postnatal day 19; Tg/Tg). NMJs were visualised with α-bungarotoxin (BTX). Scale bar = 40 μm. **D–F** Quantitative analysis of CD68+ cells in

the innervation zone of GC, TA and EDL muscles. Data is presented as mean ± sem. Data analysis: (**D**) *gastrocnemius*: $n = 4$ mice (WT, Tg/Tg), unpaired, two-tailed t-test, $p = 0.0034$; (**E**) *tibialis anterior*: $n = 3$ (WT), $n = 4$ (Tg/Tg), unpaired, two-tailed Mann-Whitney test [Shapiro-Wilk normality test, WT group: $p = 0.1555$, Tg/Tg group: $p = 0.0459$]; (**F**) extensor digitorum longus: $n = 3$ (WT, Tg/Tg), unpaired, two-tailed t-test. n.s. = non-significant; ** = $p < 0.01$.

## Proteomic characterisation of immune responses in hTDP-43Tg/Tg mice

In order to identify the specific molecular pathways driving immune cell infiltration in the affected muscles, we performed a proteomic assessment of the commonest 111 pro-inflammatory cytokines and chemokines at a late-symptomatic stage (P19) when both CD45+ and CD68+ cells showed a significant infiltration. Whole proteome from GC, TA and EDL muscles, as well as spinal cord, was compared from hTDP-43Tg/Tg mice to their WT littermates (Fig. 5A).

In the most vulnerable GC muscle, 26 inflammatory proteins were elevated and 8 were decreased (using a 25% change as cutoff threshold). Amongst these dysregulated proteins, a group of related chemokines, specifically CCL2, CCL3, CCL4, CCL5 and CCL6, showed the most notable increases (Fig. 5A). These chemokines are potent chemoattractants and can induce robust immune cell recruitment[26]. In the less vulnerable TA and EDL muscles, only 1 protein showed moderate elevation, whilst 38 (TA) and 67 (EDL) proteins had moderately decreased levels. The CCLs identified as being strongly dysregulated in GC showed a decreased expression in the TA and EDL muscles (Fig. 5A), suggesting that their increased expression was correlating directly with NMJ denervation.

Assessment of immune cell responses in spinal cord revealed 6 proteins with increased expression, and 15 proteins with decreased expression (Fig. 5A). Out of those most notably altered in the GC

muscle (CCL2, CCL3, CCL4, CCL5 and CCL6 chemokines), only CCL6 showed an increase in the spinal cord, whilst the rest remained unchanged. Thus, the profile of immune responses detected in the GC muscle represented a muscle- and denervation-specific response in the hTDP-43Tg/Tg mouse model of ALS.

Based on this initial semi-quantitative proteomic screen, we identified CCL2, CCL3, CCL4 and CCL5 chemokines as potential regulators of immune cell infiltration in the vulnerable GC muscle. To validate and confirm these findings we carried out a more sensitive and specific multiplex immunoassay-based quantitative analysis (Legendplex immunoassay). This confirmed our previous results, revealing a 10.14-fold increase in CCL2 (0.164 vs. 1.663 pg/mg, $p = 0.0350$; Fig. 5B), 5.35-fold increase in CCL3 (0.086 vs. 0.465 pg/mg, $p = 0.0174$; Fig. 5C), 2.67-fold increase in CCL4 (3.015 vs. 8.067 pg/mg, $p = 0.0209$; Fig. 5D), and a 2.77-fold increase in CCL5 levels (0.416 vs. 1.154 pg/mg, $p = 0.0031$; Fig. 5E) in the GC muscle relative to WT controls. CCL2 and CCL4 levels remained unchanged in the less vulnerable TA muscle (Fig. 5B, D), while we detected a 3.29-fold decrease in CCL3 (0.645 vs. 0.196 pg/mg, $p = 0.0318$; Fig. 5C) and a 1.75-fold decrease in CCL5 levels (1.239 vs. 0.706 pg/mg, $p = 0.0456$; Fig. 5E). In the spinal cord, only CCL3 showed a significant change, with a 4.67-fold increase (4.534 vs. 21.20, $p = 0.0083$; Fig. 5C). These results indicate a robust and selective chemokine response in the vulnerable GC muscle, paralleling the immune cell infiltration pattern.
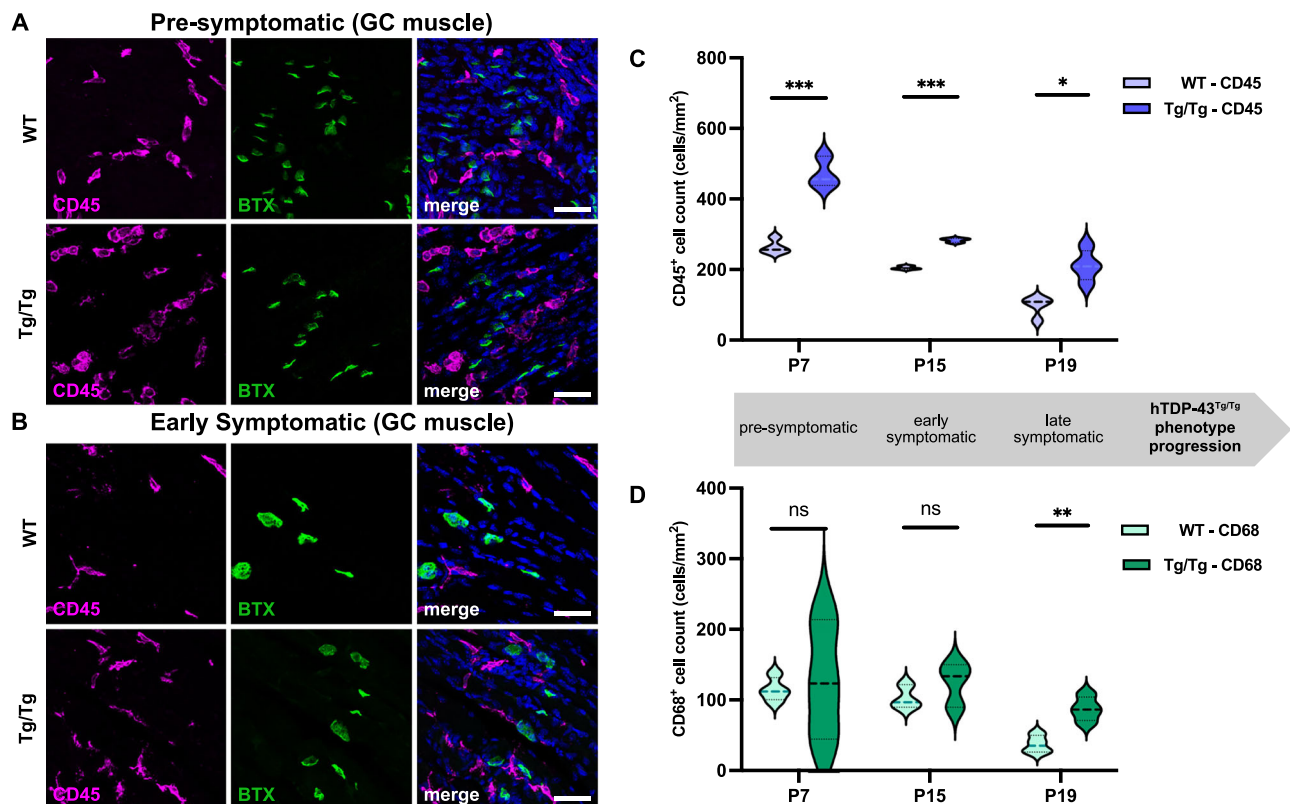
**Fig. 4 | Leukocyte infiltration at presymptomatic and early symptomatic stages in the innervation zone of the severely affected _gastrocnemius_ (GC) muscle. A, B** Immunohistochemical analysis of CD45+ leukocytes in the innervation zone of the GC muscle in presymptomatic (**A**) and early symptomatic (**B**) hTDP-43[Tg/Tg] mice (Tg/Tg) and age-matched wild-type (WT) littermates. NMJs were visualised with α-bungarotoxin (BTX), nuclei were labeled with DAPI (blue). Scale bar = 40 μm. **C** Violin plots showing quantitative analysis of CD45+ in the innervation zone of the GC muscle of presymptomatic (postnatal day 7; WT $n = 4$; Tg/Tg $n = 3$) and early symptomatic mice (postnatal day 15; WT $n = 3$; Tg/Tg $n = 3$), compared to late symptomatic mice (postnatal day 19 – data from Fig. 2). Each time point represents a separate cohort of mice. Bold dashed line represents median, thin dashed lines represent quartiles. **D** Violin plots showing quantitative analysis of CD68+ in the innervation zone of the GC muscle of presymptomatic (postnatal day 7; WT $n = 4$; Tg/Tg $n = 3$) and early symptomatic mice (postnatal day 15; WT $n = 3$; Tg/Tg $n = 3$), compared to late symptomatic mice (postnatal day 19 – data from Fig. 3). Each time point represents a separate cohort of mice. Bold dashed line represents median, thin dashed lines represent quartiles. Data analysis: (**C**) P7: unpaired, two-tailed t-test, $p = 0.0003$; (**C**) P15: unpaired, two-tailed t-test, $p < 0.0001$; (**C**) P19: two-tailed Mann-Whitney test [Shapiro-Wilk normality test, WT group: $p = 0.0328$, Tg/Tg group: $p = 0.6879$], $p = 0.0286$; (**D**) P7: unpaired, two-tailed t-test, (**D**) P15: unpaired, two-tailed t-test, (**D**) P19: unpaired, two-tailed t-test, $p = 0.0034$. n.s. = non-significant; * = $p < 0.05$; ** = $p < 0.01$; *** = $p < 0.001$.

## The CCL2-CCR2 axis is upregulated in GC muscle of hTDP-43[Tg/Tg] mice

As the CCL2 chemokine showed the greatest magnitude of increase in the GC muscle of late symptomatic hTDP-43[Tg/Tg] mice (compared to CCL3, CCL4 and CCL5), we next used immunohistochemical staining to examine the presence and localisation of CCL2+ cells. Qualitative assessment of late symptomatic GC muscle from hTDP-43[Tg/Tg] mice revealed more prominent CCL2+ cells compared to WT controls (Fig. 6A, B). CCL2 was predominantly localised in the cytoplasm (Supplementary movie 1). A substantial proportion of CCL2-expressing cells were located in the close vicinity of NMJs (Fig. 6B). CCL2 did not co-localise with either pre- (SV2a) or postsynaptic markers (α-BTX) at the NMJ (Fig. 6C, Supplementary movie 1), rather occupying a perisynaptic location. Quantification of the ratio of NMJs with perisynaptic CCL2+ cells in the GC muscle of hTDP-43[Tg/Tg] mice revealed a significant increase across all disease stages (P7: 36.3 vs. 61.7% of NMJs, $p = 0.0466$; P15: 53.0 vs. 70.1% of NMJs, $p = 0.0088$; P19: 51.3 vs. 84.9% of NMJs, $p = 0.0011$; Fig. 6D–F).

Since CCL2 functions primarily by binding to CCR2 with high affinity[13], we next evaluated CCR2+ cell expression in the GC muscle over these same disease stages. Compared to the relatively low number of CCR2+ cells in WT GC muscle (Fig. 7A), we detected a significant

increase in the number of cells in late symptomatic hTDP-43[Tg/Tg] mice (Fig. 7B). The majority of CCR2+ cells were CD45+ (Fig. 7C), indicating that these cells were leukocytes. The CCR2+ cell count was already significantly higher in early symptomatic hTDP-43[Tg/Tg] mice compared to WT controls (Fig. 7D), reaching its peak at the late symptomatic disease stage (4.88 vs. 17.03 cells/mm², $p = 0.0012$; Fig. 7F). Despite the significant increase in CCR2+ cell count, the number of CCR2+ cells was relatively low compared to the total number of CD45+ leukocytes observed. The ratio of CCR2+ cells normalised to the mean CD45+ cell count was $5.03 \pm 0.72\%$ in the WT group, however, this increased to $8.05 \pm 0.94\%$ in the late symptomatic hTDP-43[Tg/Tg] group ($p = 0.044$, unpaired, two-tailed t-test). Whilst this suggests that multiple pro-inflammatory and chemotactic pathways are being upregulated, the observed shift in the CCR2/CD45 ratio confirms an important contribution of the CCL2-CCR2 pathway in this process.

To validate the clinical translatability and relevance of these CCR2-dependent pathways, we quantified the number of CCR2+ cells in skeletal muscle from ALS patients. In healthy control individuals, we observed a minimal presence of CCR2+ cells (Fig. 7G). In stark contrast, we found a clear increase in the number of CCR2+ cells in ALS patient skeletal muscle (1.091 vs. 7.087 cells/mm², $p = 0.0038$; Fig. 7H, I), revealing partial co-localisation with the leukocyte marker CD45. This
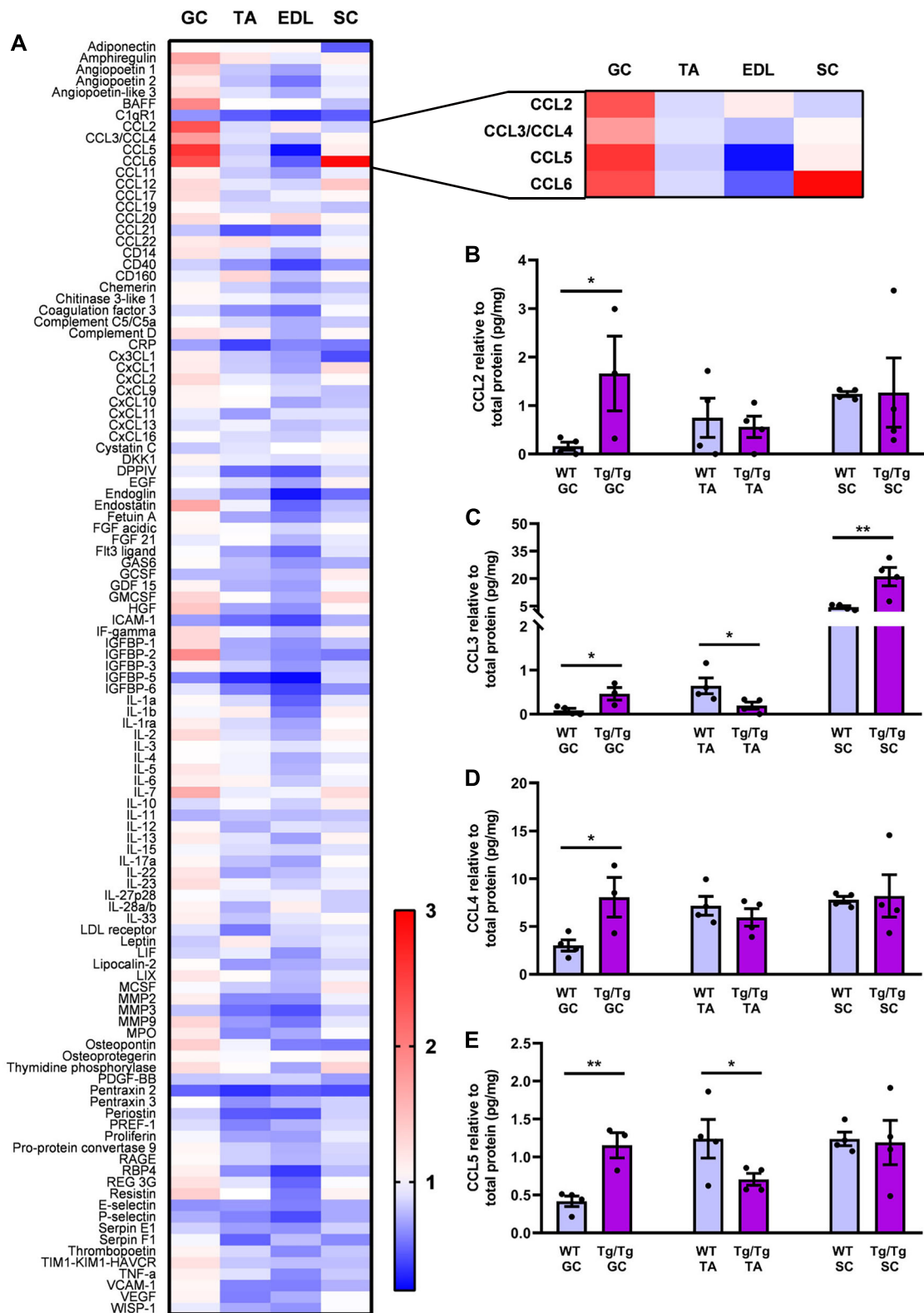
**Fig. 5 | Proteomic characterisation of inflammatory responses in hTDP-43^{Tg/Tg} mice. A** Proteome profiler analysis of 111 inflammatory proteins in *gastrocnemius* (GC), *tibialis anterior* (TA) and *extensor digitorum longus* (EDL) muscles and spinal cord (SC) samples from late symptomatic (postnatal day 19) hTDP-43^{Tg/Tg} mice. Fold change in protein levels is presented relative to wild-type (WT) littermate controls. In the GC muscle, CCL2, CCL3, CCL4, CCL5 and CCL6 chemokines showed the greatest increase in protein levels (magnified and highlighted in the top right panel). Exact fold changes are available in the Source Data file. **B**–**E** Quantitative analysis of CCL2 (**B**), CCL3 (**C**), CCL4 (**D**) and CCL5 (**E**) proteins in the GC and

TA muscles and SC using Legendplex immunoassay. Data is presented as mean ± sem. The Legendplex multiplex immunoassay and statistical analysis was performed with $n = 4$ mice in the GC, TA and SC of the WT group and TA and SC of the Tg/Tg group. The GC of the Tg/Tg group was quantified in $n = 3$ mice. Data analysis: In each case (**B**–**E**), unpaired, one-tailed t-test was performed for direct comparison of WT vs Tg/Tg groups; (**B**) *gastrocnemius*: $p = 0.0350$; (**C**) g*astrocnemius*: $p = 0.0174$; (**C**) *tibialis anterior*: $p = 0.0318$; (**C**) *spinal cord*: $p = 0.0083$; (**D**) *gastrocnemius*: $p = 0.0209$; (**E**) *gastrocnemius*: $p = 0.0031$; (**E**) *tibialis anterior*: $p = 0.0456$. * = $p < 0.05$; ** = $p < 0.01$.
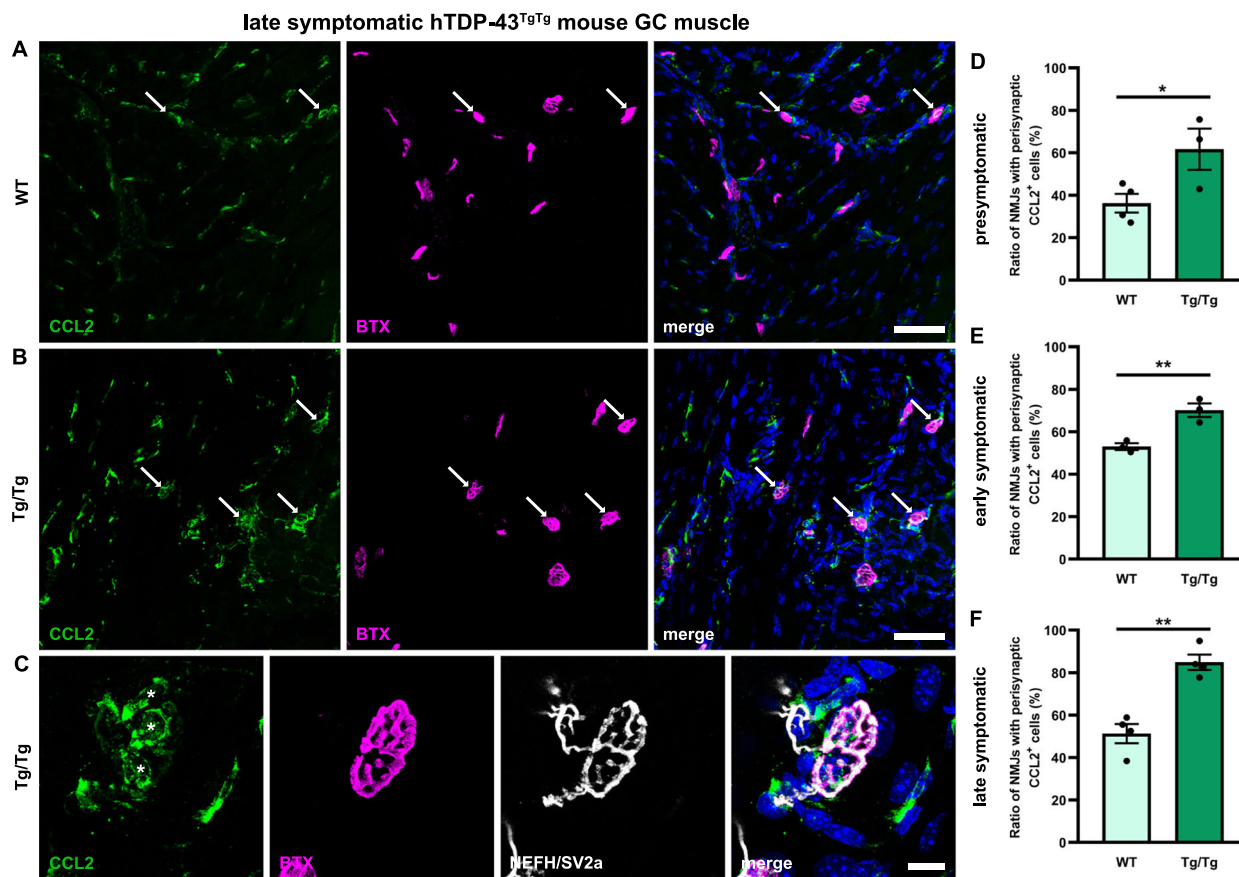
**Fig. 6 | CCL2 expression in the *gastrocnemius* (GC) muscle across different disease stages. A–C** CCL2 staining (green) in the GC muscle of wild-type (WT; **A**) and late symptomatic postnatal day 19 (P19) hTDP-43[Tg/Tg] (Tg/Tg; **B, C**) mice. Arrows indicate CCL2^{+} cells in the close vicinity of neuromuscular junctions (NMJs), visualised with α-bungarotoxin (BTX; magenta). **C** High magnification image of CCL2^{+} cells around a single NMJ in the GC muscle of late stage hTDP-43[Tg/Tg] mice. Innervation is shown through NEFH/SV2a (gray) staining. Asterisks label individual nuclei of CCL2^{+} cells. 3D-reconstructed version of this image is available as

Supplementary movie 1. **D–F** Quantitative analysis of the ratio of NMJs with peri-synaptic CCL2-expressing cells in presymptomatic (**D**), early symptomatic (**E**) and late symptomatic (**F**) mice. Data is presented as mean ± sem. Scale bar represents 50 μm on (**A, B**) and 10 μm on (**C**). Data analysis: (**D**) Presymptomatic stage (post-natal day 7): $n = 4$ (WT), $n = 3$ (Tg/Tg), unpaired, two-tailed t-test, $p = 0.0466$; (**E**) Early symptomatic stage (postnatal day 15): $n = 3$ (WT, Tg/Tg), unpaired, two-tailed t-test, $p = 0.0088$; (**F**) Late symptomatic stage: $n = 4$ (WT, Tg/Tg), unpaired, two-tailed t-test, $p = 0.0011$. * = $p < 0.05$; ** = $p < 0.01$.

confirms that the CCR2 pathway is dysregulated in skeletal muscle of ALS patients, substantiating our previous findings in the hTDP-43[Tg/Tg] mouse model.

## Local CCL2 neutralisation or IgG treatment reduces leukocyte infiltration and ameliorates NMJ pathology
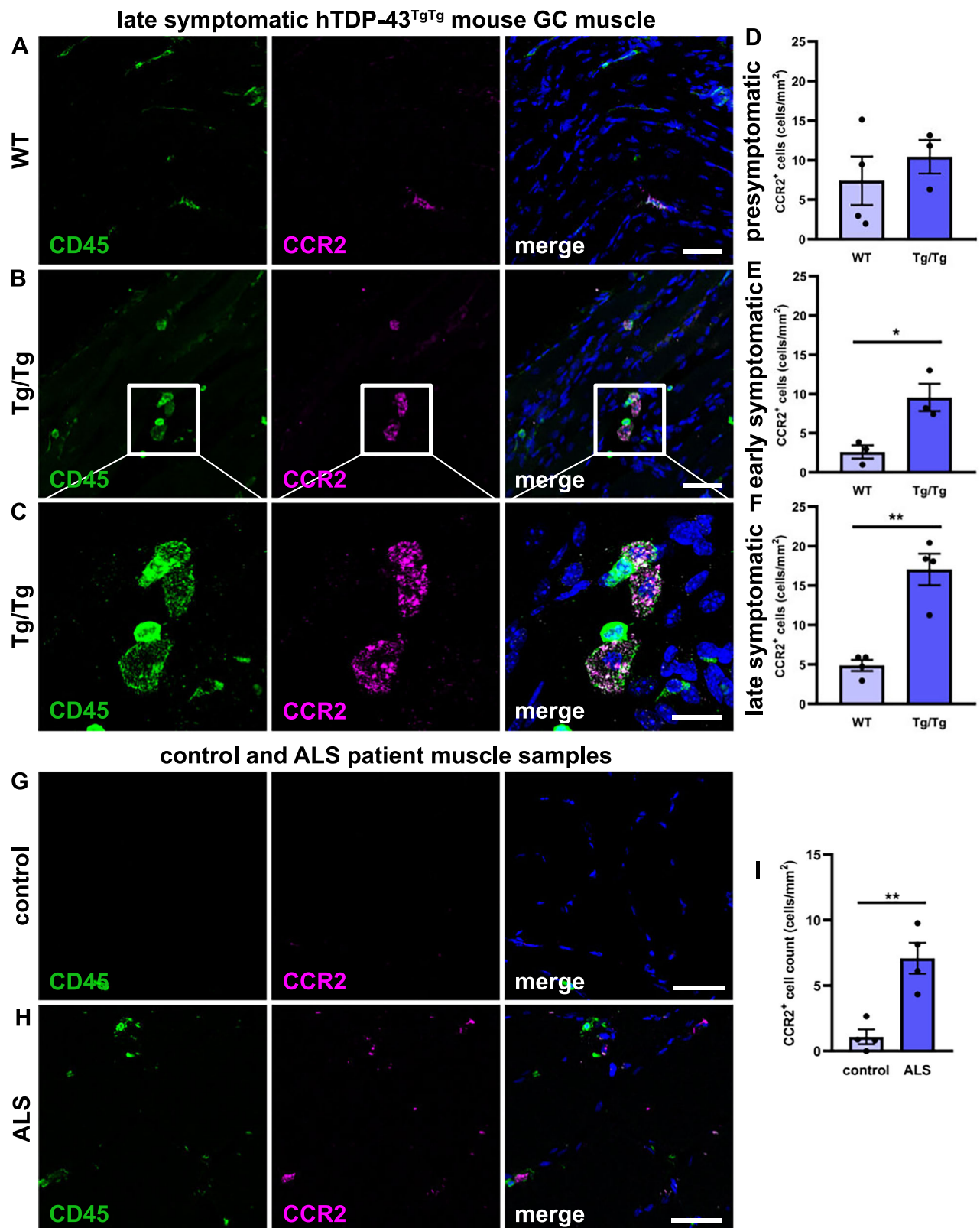
Given the identification of the CCL2-CCR2 axis, and consequent immune cell responses, as a major driver of immunological changes in ALS muscle with high levels of NMJ denervation, we next wanted to establish whether targeting these pathways may represent a viable therapeutic option. Direct CCL2 neutralisation represents a targeted therapy of a single chemokine pathway, while a relatively high-dose normal immunoglobulin G (IgG) treatment targets multiple inflam-matory pathways, including the CCL2 response[27,28].

Although both CCL2 neutralisation and IgG treatment can be administered in high doses to achieve a systemic effect, we reasoned that such an approach is not likely to be ideal for ALS therapeutics. For example, long-term CCL2 neutralisation has been shown to induce increased (likely compensatory) expression of CCL2 in vivo[29]. Similarly, systemic high-dose IgG treatment can cause temporary elevation of CCL2 expression[28]. Since our results indicated that the CCL2-CCR2 pathway is only being significantly upregulated in the most severely affected muscles, we hypothesised that a targeted, local therapeutic

intervention would be more likely to succeed. Moreover, by delivering intramuscular treatment to a single affected muscle, it is possible to use the contralateral (uninjected) muscle as an internal control, allowing us to identify and exclude any systemic compensatory responses. Thus, we microinjected CCL2-neutralising or isotypic nor-mal goat IgG antibodies into the GC muscle of hTDP-43[Tg/Tg] mice at P7 and P15. Mice were monitored until a late symptomatic stage (P19), where the injected GC muscle was analysed for progression of neu-romuscular phenotypes and immune cell infiltration compared to the contralateral uninjected control (Fig. 8A).

Denervation analysis revealed that only 41.67% of NMJs were fully innervated in the contralateral, uninjected GC muscle of ALS mice (Fig. 8B, H), corresponding to levels reported previously in untreated hTDP-43[Tg/Tg] mice[22]. This suggested that local intramuscular treatment had not spread systemically, nor impacted on global neuromuscular pathology. Strikingly, in contrast we found a significantly higher number of innervated NMJs in both treatment groups (IgG: 69.77%, $p < 0.0001$; CCL2: 66.35%, $p < 0.0001$; Fig. 8C, D, H). This indicates a robust neuroprotective effect on NMJs resulting from both antibody-based local immunomodulatory treatments.

To obtain a more in-depth understanding of the subcompart-mental NMJ alterations occurring in these mice, we conducted quan-titative morphometric analysis using the ImageJ plug-in NMJ Morph[30].
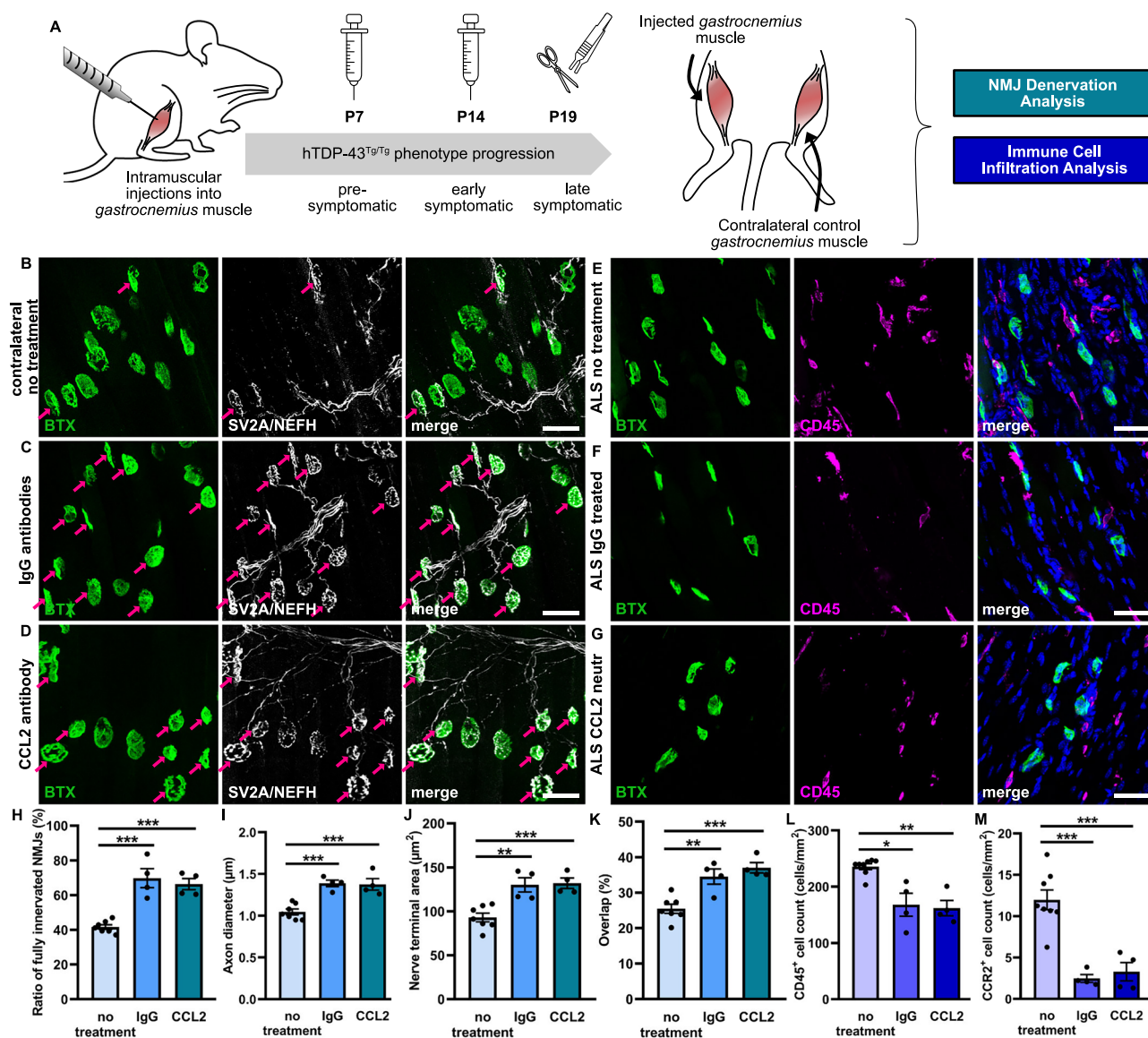
**late symptomatic hTDP-43$^{TgTg}$ mouse GC muscle**

A — WT: CD45, CCR2, merge
B — Tg/Tg: CD45, CCR2, merge
C — Tg/Tg: CD45, CCR2, merge

D — presymptomatic: CCR2$^+$ cells (cells/mm$^2$), WT vs Tg/Tg
E — early symptomatic: CCR2$^+$ cells (cells/mm$^2$), WT vs Tg/Tg, *
F — late symptomatic: CCR2$^+$ cells (cells/mm$^2$), WT vs Tg/Tg, **

**control and ALS patient muscle samples**

G — control: CD45, CCR2, merge
H — ALS: CD45, CCR2, merge

I — CCR2$^+$ cell count (cells/mm$^2$), control vs ALS, **

This tool allows for quantitative, objective comparison of both pre- and postsynaptic parameters at individual NMJs. We have previously shown that the hTDP-43$^{Tg/Tg}$ model has a clear presynaptic phenotype with a significantly smaller nerve terminal area and perimeter compared to WT controls[22]. NMJ Morph analysis revealed that in both antibody-treated groups, presynaptic parameters such as axon diameter, nerve terminal area, nerve terminal perimeter and complexity were all significantly improved compared to untreated animals (Table 2). Furthermore, the area of synaptic contact and the derived overlap also showed robust improvement (Table 2). In contrast, the postsynaptic parameters (AChR area, AChR perimeter, endplate area, endplate perimeter, compactness and fragmentation) remained unchanged following antibody treatment (Table 2). These parameters are not predicted to be affected in hTDP-43$^{Tg/Tg}$ due to the neuronal-

**Fig. 7 | Activation of the CCR2 pathway in ALS patients and in the hTDP-43$^{Tg/Tg}$ mice across different disease stages. A–C** CCR2 staining in the GC muscle of wild-type (WT; **A**) and late symptomatic (postnatal day 19) hTDP-43$^{Tg/Tg}$ mice (Tg/Tg; **B**, **C**). **C** High magnification image reveals co-expression of CCR2 and CD45 markers, however, not all of the CD45$^+$ cells show CCR2 staining. **D–F** Quantitative analysis of CCR2$^+$ cells in the GC muscle of presymptomatic (**D**), early symptomatic (**E**) and late symptomatic (**F**) hTDP-43$^{Tg/Tg}$ mice. **G–H** CCR2 staining in the skeletal muscle of control individuals (control; **G**) and ALS patients (ALS; **H**).

**I** Quantification of CCR2$^+$ cells in the skeletal muscle of healthy control (CTRL-2 in Table 1) and ALS patient (ALS-1 in Table 1) muscle samples. Data is presented as mean ± sem. Scale bar represents 50 μm on (**A, B**), 20 μm on (**C**) and 40 μm on (**G, H**). Data analysis: (**D**) Presymptomatic stage: $n = 4$ (WT), $n = 3$ (Tg/Tg), unpaired, two-tailed t-test; (**E**) Early symptomatic stage: $n = 3$ (WT, Tg/Tg), unpaired, two-tailed t-test, $p = 0.0234$; (**F**) Late symptomatic stage: $n = 4$ (WT, Tg/Tg), unpaired, two-tailed t-test, $p = 0.0012$; (**I**) Human muscle samples: $n = 4$ (control, ALS), unpaired, two-tailed t-test, $p = 0.0038$. * = $p < 0.05$; ** = $p < 0.01$.



**Fig. 8 | Local intramuscular CCL2 neutralisation or IgG treatment ameliorates NMJ pathology and reduces immune cell infiltration in the GC muscle of hTDP-43$^{Tg/Tg}$ mice. A** Schematic of experimental design. **B–D** Representative images of NMJ denervation in the *gastrocnemius* (GC) muscle of untreated (**B**), IgG-treated (**C**) and CCL2-neutralising antibody-treated (**D**) late symptomatic postnatal day 19 (P19) hTDP-43$^{Tg/Tg}$ mice. Red arrows indicate fully innervated NMJs, as revealed by the presynaptic NEFH/SV2a staining. Scale bar represents 40 μm. **E–G** Representative images of the CD45$^+$ leukocyte infiltration in the innervation zone of the GC muscle in untreated (**E**), IgG-treated (**F**) and CCL2-neutralising antibody-treated (**G**) late symptomatic hTDP-43$^{Tg/Tg}$ mice. Scale bar represents 40 μm. **H** Qualitative analysis of NMJ innervation, representing the ratio of fully innervated NMJs in the GC muscle. Analysis was performed with $n = 7$ (untreated) and $n = 4$ (IgG, CCL2) mice/group and one-way ANOVA with Fisher's LSD post-hoc, no treatment vs. IgG:

$p < 0.0001$, no treatment vs. CCL2: $p < 0.0001$. On average 30-40 NMJs were analysed per muscle. **I–K** Quantitative morphometric analysis of the NMJs revealed improvement in axonal diameter (**I**), nerve terminal area (**J**) and overlap (**K**) variables. The exact p values and statistical analyses are detailed in Table 2. **L, M** Quantitative analysis of CD45$^+$ (**L**) and CCR2$^+$ (**M**) cell count in the late symptomatic GC muscle of hTDP-43$^{Tg/Tg}$ mice. Analysis was performed on $n = 8$ (untreated) and $n = 4$ (IgG, CCL2) mice/group. Data analysis: (**L**) CD45 analysis: Kruskal-Wallis test and uncorrected Dunn's post-hoc [Shapiro-Wilk normality test, ALS untreated group: $p = 0.0091$, ALS IgG group: $p = 0.7802$, ALS CCL2 group $p = 0.3820$], no treatment vs. IgG: $p = 0.0114$, no treatment vs. CCL2: $p = 0.0053$; (**M**) CCR2 analysis: one-way ANOVA with Fisher's LSD post-hoc, no treatment vs. IgG: $p < 0.0001$, no treatment vs. CCL2: $p = 0.0002$. * = $p < 0.05$; ** = $p < 0.01$; *** = $p < 0.001$. Data is presented as mean ± sem.

**Table 2 | Morphometric parameters of NMJs in untreated, IgG- and CCL2 neutralising antibody-treated GC muscles**

| Morphometric parameters | | ALS untreated | ALS IgG-treated | ALS CCL2 neutr. |
|---|---|---|---|---|
| **Presynaptic parameters** | Axon diameter (µm) | 1.05 ± 0.09 | **1.39 ± 0.08 (p = 0.0002)** | **1.37 ± 0.14 (p = 0.0003)** |
| | Nerve terminal area (µm²) | 93.07 ± 13.15 | **130.10 ± 16.32 (p = 0.0010)** | **131.99 ± 11.76 (p = 0.0007)** |
| | Nerve terminal perimeter (µm) | 169.25 ± 22.94 | **235.22 ± 24.08 (p = 0.0004)** | **225.51 ± 15.65 (p = 0.0014)** |
| | Nerve terminal complexity (a.u.) | 4.63 ± 0.17 | **5.11 ± 0.30 (p = 0.0022)** | **4.95 ± 0.07 (p = 0.0238)** |
| **Postsynaptic parameters** | AChR area (µm²) | 351.31 ± 43.06 | 375.75 ± 31.99 | 349.90 ± 26.27 |
| | AChR perimeter (µm) | 128.54 ± 14.80 | 137.80 ± 25.70 | 125.48 ± 8.82 |
| | Endplate area (µm²) | 415.26 ± 47.01 | 440.30 ± 38.71 | 415.30 ± 31.45 |
| | Endplate perimeter (µm) | 85.28 ± 5.37 | 87.42 ± 4.86 | 84.37 ± 3.42 |
| | Endplate diameter (µm) | 33.02 ± 2.82 | 32.71 ± 1.78 | 32.17 ± 2.98 |
| | Compactness (a.u.) | 84.51 ± 1.37 | 85.34 ± 1.78 | 84.37 ± 1.32 |
| | Fragmentation (a.u.) | 0.12 ± 0.06 | 0.12 ± 0.10 | 0.11 ± 0.05 |
| **Others** | Area of synaptic contact (µm²) | 88.45 ± 12.45 | **125.43 ± 15.33 (p = 0.0005)** | **127.77 ± 9.34 (p = 0.0003)** |
| | Overlap (%) | 25.45 ± 3.38 | **34.54 ± 4.27 (p = 0.0014)** | **37.03 ± 2.92 (p = 0.0002)** |

Values represent mean ± sem. Statistically significant differences are highlighted in bold, with $p$ values. In each case, treated groups were compared to the untreated contralateral values. Statistical analysis was performed with $n = 7$ (untreated) and $n = 4$ (IgG, CCL2) mice/group. 30-40 NMJs were analysed per muscle. Based on normality tests, parametric one-way ANOVA with Fisher's LSD post-hoc was used out for axon diameter, nerve terminal area, nerve terminal perimeter, nerve terminal complexity, AChR area, endplate area, endplate perimeter, endplate diameter, fragmentation, area of synaptic contact and overlap variables and Kruskal-Wallis test with uncorrected Dunn's post-hoc was used for AChR perimeter [Shapiro-Wilk normality test, ALS untreated group: $p = 0.0244$, ALS IgG group: $p = 0.8536$, ALS CCL2 group $p = 0.5031$] and compactness [Shapiro-Wilk normality test, ALS untreated group: $p = 0.9778$, ALS IgG group: $p = 0.4864$, ALS CCL2 group $p = 0.0381$]. $a.u$ = arbitrary unit, $neutr$ = neutralisation.

specific promoter (Thy1) used to drive transgene expression. These results therefore confirm that the intramuscular antibody injection did not have a detrimental effect on postsynaptic/muscle morphology.

Finally, in order to assess whether this rescue of NMJ pathology was being achieved via modulation of the immune pathways identified earlier in the study, we quantified the number of infiltrating CD45^{+} leukocytes. The leukocyte cell count in the untreated contralateral GC muscle was indistinguishable from the previously described CD45 cell count in the GC muscle of untreated P19 hTDP-43[Tg/Tg] mice (Figs. 3A and 8E; 235.67 [contralateral GC innervation zone] vs. 211.6 [P19 hTDP-43[Tg/Tg] GC innervation zone]), indicating that the local treatment protocol did not influence immune cell infiltration into the contralateral GC muscle. Compared to the untreated contralateral side (Fig. 8E), both IgG (Fig. 8F) and CCL2 neutralisation (Fig. 8G) reduced the number of leukocytes in the innervation zone of the GC muscle [235.67 (untreated) vs. 168.09 (IgG) ($p = 0.0114$) and 162.02 (CCL2) ($p = 0.0053$) cells/mm²; Fig. 8L]. The CD45^{+} leukocyte count remained unchanged in the non-innervation zone of the GC muscle in both treatment groups [150.89 (untreated) vs. 121.71 (IgG) ($p = 0.0650$) and 157.76 (CCL2) ($p = 0.6994$) cells/mm²; Supplementary Fig. 5]. We also observed a reduction in the number of CCR2^{+} cells in both treatment groups [11.97 (untreated) vs. 2.482 (IgG) ($p < 0.0001$) and 3.294 (CCL2) ($p = 0.0002$) cells/mm²; Fig. 8M]. These results indicate that the NMJ-protecting effect of both CCL2 neutralisation and IgG treatment correlated with a direct reduction in the number of infiltrating immune cells.

## Discussion

Immune dysregulation and overactivation of inflammatory pathways are characteristic features of ALS pathophysiology. The importance of inflammatory processes is also evidenced by ongoing clinical trials featuring targeted modulation of the immune dysregulation in ALS patients, such as the autologous $T_{reg}$ expansion therapy (NCT06307301)[31] or the tyrosine-kinase inhibitor masitinib treatment (NCT03127267)[32]. Despite these efforts, none of the previous anti-inflammatory treatment trials have identified a clear benefit in the clinical setting, and it is still unclear how inflammatory processes precisely contribute to motor neuron pathology and disease pathogenesis[9]. Here, we have demonstrated robust leukocyte infiltration in the skeletal muscle as a major immune-related phenotype in

ALS patients which was consistently recapitulated across three independent ALS mouse models, regardless of age of onset or speed of disease progression. A portion of these infiltrating cells were identified as macrophages in the skeletal muscle of hTDP-43[Tg/Tg] mice, and this infiltration was present from before the onset of overt neuromuscular pathology. We identified the CCL2-CCR2 axis as a mediator of this process and showed that local administration of CCL2-neutralising or normal IgG antibodies rescues NMJ denervation and ameliorates immune cell infiltration in hTDP-43[Tg/Tg] mice.

Resident and infiltrating immune cells in skeletal muscle play an essential role in repair and pathogen clearance, however, their abundance and function is altered in several pathological states (e.g., myopathies, acute injuries)[33]. While immune cells might support the restoration of NMJ structure and function in acute injury[34], the chronic overactivation of macrophages hastens NMJ denervation[35]. Here we found an increased number of CD45^{+} leukocytes in skeletal muscle samples from ALS patients, suggestive of increased immune activity in these affected muscles. In the hTDP-43[Tg/Tg] mouse model of ALS, we found a similar infiltration of CD45^{+} leukocytes and CD68^{+} macrophages in skeletal muscle, demonstrating that this acute disease model recapitulates the intramuscular inflammatory processes observed in ALS patients. In hTDP-43[Tg/Tg] mice, the immune cells were primarily localised in the innervation zone of the muscles and both leukocyte and macrophage infiltration were more pronounced in the highly affected GC muscle, compared to the moderately affected TA and EDL muscles. In the GC muscle, the increased leukocyte count was already detectable presymptomatically, suggesting that immune cell influx and/or proliferation precedes NMJ denervation. Their preferential perisynaptic localisation also suggests a direct interaction with the neuronal, glial and/or muscle cells coming together to form each NMJ.

Proteomic analysis of late symptomatic hTDP-43[Tg/Tg] muscle samples identified a group of upregulated chemokines (CCL2, CCL3, CCL4, and CCL5), specific to the highly affected GC muscle. These chemokines are considered to have prominent chemotactic and pro-inflammatory qualities[26], thus they are well-placed to induce the kind of immune cell infiltration observed in hTDP-43[Tg/Tg] mice. One of these chemokines in particular, CCL2, was primarily expressed in cells localised in close vicinity to NMJs. Furthermore, we also found an increase in the number of CCR2^{+} cells in the GC muscle, already evident at presymptomatic disease stages. The CCL2-CCR2 axis has already been implicated in the pathogenesis of other conditions where NMJs

are a primary pathological target. For example, in Guillain-Barré syndrome (GBS), infiltrating CCR2$^+$ cells were observed in GBS patients[36]. Increased CCL2 levels have also been reported in the peripheral nerve and spinal cord of both slow- and fast-progressing 129SvSOD1$^{G93A}$ mouse models of ALS[37]. Besides the role of CCL2-CCR2 axis in nerve tissue, it has been reported that the inhibition of CCR2 signaling promotes regeneration of aged muscle following acute muscle injury, suggesting that the pathway might also directly impact myogenesis[38].

In an earlier study, self-complementary adeno-associated virus (scAAV)9 vector-induced intramuscular overexpression of CCL2 worsened motor function in the fast-progressing 129SvSOD1$^{G93A}$ mouse model of ALS[37]. This finding provides strong support for the results presented here suggesting that the CCL2-CCR2 axis represents a mediator of neuromuscular pathology that is amenable to therapeutic intervention. We were able to elicit robust neuroprotective effects using either single-target (CCL2-specific) or multi-target immunomodulation with IgG antibodies in local treatment paradigms. Both treatments improved NMJ innervation, ameliorated leukocyte infiltration and reduced the number of CCR2$^+$ cells in affected muscles. Since this treatment was injected into a single muscle, we only observed a local effect on the NMJs of the *gastrocnemius*. This would make it challenging to assess whether the immunomodulatory treatment had an effect on overall function of the hindlimb, for example through motor behavior or grip strength assessment, and is a limitation to these conclusions. Further work investigating administration of immunomodulation to multiple muscles should focus on the impact of NMJ preservation on motor performance.

Since we observed a reduction in immune cell infiltration following local immunomodulatory treatment, we conclude that blockade of the CCL2-CCR2 axis was preventing immune cells from targeting pathological NMJs. One potential limitation of these experiments using the hTDP-43$^{Tg/Tg}$ mouse model is that pathological changes are induced at a time coinciding with natural postnatal maturation of the neuromuscular system. Thus, it is possible that immunomodulatory treatments were targeting underlying developmental pathways in the hTDP-43$^{Tg/Tg}$ animals, as well as (or instead of) ALS-associated neurodegenerative pathways. Equally, the CCL2-CCR2 axis, as well as acting on cell recruitment and activation, has been shown to act through molecular pathways related to cell survival, such as the BDNF-TrkB pathway[39] or the PI3K-Akt pathway[40]. Further research is therefore warranted to investigate the exact mechanism(s) by which blocking the CCL2-CCR2 axis protects NMJs.

Systemic intravenous delivery of high-dose IgG (IVIG) has been evaluated previously in two clinical trials of ALS patients, with both failing to improve clinical outcomes[41,42]. Although these studies were performed on a very small scale (7 and 9 patients participated) and conducted without any placebo control groups, they support our decision to adopt a local targeting approach for CCL2-CCR2 pathway in place of a non-targeted, systemic IVIG treatment. Intramuscular neutralisation of the CCL2-CCR2 pathway specifically blocks the immune cell interactions at the NMJ without interfering with any other roles that this axis may play in the immune system, whilst also potentially limiting any compensatory responses. Taken together with the multitude of unsuccessful ALS-related clinical trials that have been reported over recent years, it appears that refined, targeted, and possibly combinatorial treatment options are going to be required to successfully target the complex pathophysiology of ALS. Our approach of a targeted, local manipulation of immune responses may therefore offer a route to directly manipulate NMJ denervation, highlighting an attractive area for therapy development.

## Methods

### Study design

We conducted the initial quantification of leukocyte and macrophage infiltration in the skeletal muscle of control individuals and ALS patients. We excluded muscle samples from clinically slow-progressing patients. We then assessed whether this immune infiltration phenotype was recapitulated in three ALS mouse models: severe early-onset (hTDP-43$^{Tg/Tg}$: RRID:IMSR_JAX:012836), fast progressive adult-onset (TDP-43$^{A315T}$: RRID:IMSR_JAX:010700) and slow progressive adult-onset (TDP-43$^{M337V}$: RRID:IMSR_JAX:029266). Next, for further in-depth characterisation we used the established and well-characterised hTDP-43$^{Tg/Tg}$ (RRID:IMSR_JAX:012836) murine transgenic model of ALS[43] to investigate immune cell responses and neuromuscular pathology in vivo. Based on previously reported details concerning disease progression, we collected samples at presymptomatic (P7), early symptomatic (P15) and late symptomatic (P19) disease stages[22]. WT littermates were used as controls throughout. To evaluate the potential beneficial effect of modulating the CCL2-CCR2 pathway in a severely affected muscle, we carried out local intramuscular treatments with CCL2 neutralising antibodies and normal IgG, where the predefined primary endpoint was the level of NMJ denervation. During these experiments, the animals received two intramuscular injections (at P7 and P14), with antibody dosage that corresponded to previously published experiments[44]. Since we did not expect (and also confirmed the lack of) systemic treatment effects in these mice, the contralateral muscles were used as internal control samples. The use of this local intramuscular experimental setup with contralateral internal control samples allowed us to examine the effects of a targeted treatment delivery, without multiple different off-target effects of a systemic treatment paradigm. We defined the endpoint of the treatment experiment as the late symptomatic disease stage (P19).

For each experimental litter, the homozygous (diseased) mice were randomly distributed among the different treatment groups. Multiple litters and random proportions of male and female hTDP-43$^{Tg/Tg}$ mice were used in each experiment. Male and female TDP-43$^{A315T}$ mice show different disease course, as male mice display more progressive motor phenotype and have a shorter life span[23]. Thus, to increase homogeneity, only male mice were included for experiments on TDP-43$^{A315T}$ mice. Similarly, only male WT littermate controls were included. The sample size in each experiment and experimental group was initially planned based on the accepted norms, practices and considerations for humane animal welfare guidelines (3Rs principle), with $n = 3-5$ animals/experimental group. In each case, post-hoc power analysis was carried out with G* Power (RRID:SCR_013726). The number of animals in an experimental group was not altered on a post-hoc basis. The functional decline of the animals was monitored on a daily basis with a clinical scoring system[45]. As a prospective rule, animals were to be culled before the endpoint of the experiment if they reached clinical end-stage (corresponding to the humane endpoint). However, this did not occur throughout the experiments.

The sampling and evaluation protocol for the immunohistochemical analysis of different antigens (CD45, CD68, CCR2, CCL2) in skeletal muscle was based on our previous experiments: from each muscle, we aimed to capture 10 fields of views, across different regions of the selected muscle. In a few cases (up to 10% of all muscle samples) it was not feasible to achieve this number of technical replicates, due to limited availability of sections (most commonly in the EDL muscle). In these cases, we managed to capture a minimum of 5 images per muscle. NMJ evaluation was based on a previously published protocol[30], thus we collected and analysed 30-40 *en-face* NMJs in each muscle. As for the screening of the pro-inflammatory cytokines and chemokines, due to the limited protein content in each sample, we carried out the proteome profiling experiments with pooled samples. The quantitative analysis of the selected chemokines was conducted from individual samples, with two parallel technical replicates.

For each experiment, we have included all collected data in our analysis and applied no data exclusion criteria. Outlier analysis was performed with GraphPad Prism (version 8.0.1.244, RRID:SCR_002798,

GraphPad Software, San Diego, CA, USA), with pre-defined parameters. No outliers were identified and excluded. All experiments were performed in a blinded manner: during the characterisation of slow immune response, the investigators were blinded to the genotype of the animals, while during the interventional experiments, the investigators were blinded to the treatment groups and randomisation scheme.

## Ethical approval
Samples and clinical data from patients included in this study were provided by the Basque Biobank (www.biobancovasco.org) and processed following standard procedures with appropriate approval by the Clinical Research Ethics Committees of the Basque Country and Donostia University Hospital (codes: PI2016075 and PI2021050). Written informed consent was obtained from all the subjects. This research project was conducted following the requirements of the European Regulation of Data Protection and Digital Rights guarantee. All samples were anonymised, only keeping the necessary gender and age information.

Ethical approval for the animal experiments on the hTDP-43 and TDP-43[M337V] mice was given by internal institutional review boards at the University of Edinburgh (project licence number PP1567597). Ethical approval for the animal experiments on the TDP-43[A315T] mice was given by (1) The Government Office in Csongrád-Csanád County, Hungary, and (2) The Committee for Animal Experiments of the University of Szeged (XI./640/2025). All experiments were carried out in accordance with the University of Edinburgh, University of Szeged and UK Home Office regulations, that also conforms to international laws and policies (EEC Council Directive 86/609, OJL 358 1 DEC. 12, 1987; NIH Guide for the Care and Use of Laboratory Animals, United States National Research Council, revised 1996). All efforts were made to minimise animal suffering.

## Patient information
Neurologists from the ALS Unit of Donostia University Hospital handled the patients, established the diagnoses, and performed the muscle biopsies. Skeletal muscle samples were evaluated from 4 healthy control individuals and 4 ALS patients. For the ALS patients, we applied the following exclusion criteria: I) Patients with clinically slow-progressing disease phenotypes were excluded; II) Patients with autoimmune or other immune-related co-morbidities were excluded. Control and ALS groups were sex- and age-matched (male $n = 2$, female $n = 2$ per group, control group age range at biopsy 43-75 years old, ALS patient age range at biopsy 48-71 years old). Patient information is detailed in Table 1.

## Experimental animals and treatment protocols
The TDP-43[M337V] mice and hTDP-43[Tg/Tg] mice were maintained and bred at the University of Edinburgh, while the TDP-43[A315T] mice were maintained and bred at the University of Szeged. TDP-43[M337V] mice (RRID:IMSR JAX:029266) were maintained on the C57BL/6 J background (Fig. 2 $n = 3$; 1 male, 2 female). Disease progression in males and females of the TDP-43[M337V] model is similar so the group was evenly split. TDP-43[A315T] mice (RRID:IMSR JAX:010700) were maintained on the C57BL/6 J background (Fig. 2 $n = 5$; 5 males). Male TDP-43[A315T] mice display a more aggressive disease progression and so only males were used. hTDP-43[Tg/Tg] (RRID:IMSR JAX:012836) were maintained on the FVB/N background and used as follows: Figs. 2, 3 (same mice used) $n = 4$ per group (2 male, 2 female); Figs. 4, 6 (same mice used) $n = 4$ (2 male, 2 female) vs $n = 3$ (2 male, 1 female) (WT:Tg/Tg) at P7, $n = 3$ per group (1 male, 2 female) at P15; Fig. 5 $n = 3$ per group (1 male, 2 female); Fig. 8 $n = 4$ per treatment group (2 male, 2 female per group). Due to the early time points used in the hTDP-43[Tg/Tg] model, sex does not play a factor in disease progression, so was evenly split across groups. A total of 35 hTDP-43[Tg/Tg] mice used. Mice were kept in a 14/10-hour light/ dark cycle, at 20 °C with 50% humidity, under standard specific pathogen-free conditions. Tissue was collected from fast progressive adult-onset male TDP-43[A315T] mice at late-symptomatic P90 and slow progressive adult-onset TDP-43[M337V] at early-symptomatic 12 months. For the severe early-onset hTDP-43[Tg/Tg] model, day of birth was considered P1, and the mice were sacrificed on P7 (presymptomatic), P14 (early symptomatic) or P19 (symptomatic), corresponding to the different disease stages described previously[22]. Ages of mice per experiment are detailed in the figure legends. Genotyping was carried out from ear notch samples in most cases, whilst in the treated groups mice were tail tipped and genotyped at P2. Mice homozygous for the transgene (referred to as Tg/Tg) were monitored daily for body weight and clinical scoring[45]. WT littermates were used as controls. Mice used for the characterisation of the immune response in the various skeletal muscles received no treatment intervention. To assess the effects of local immunomodulatory treatment on NMJ denervation and immune cell infiltration, hTDP-43[Tg/Tg] mice received two intramuscular injections (at P7 and P14) of either CCL2 neutralising antibody [Cat# AF-479-NA, RRID: AB_354500, R&D Systems, Minneapolis, MN, USA; 0.4 mg/kg body weight, at the concentration of 0.2 mg/ml, diluted in phosphate buffer saline (PBS)] or isotypic normal goat IgG (Cat# AB-108-C, RRID:AB_354267, R&D Systems; 0.4 mg/kg body weight, at the concentration of 0.2 mg/ml, diluted in PBS) in the severely affected GC muscle. Briefly, the mouse was restrained and the hindlimb held in a flexed position. The GC muscle was injected from the lateral aspect of the limb at a 45° angle, no deeper than 2 mm.

At the end of the experiments, mice were euthanised via overdose of anaesthetic (isoflurane). For immunohistochemistry, GC, TA, and EDL muscle samples were removed and fixed for 30 minutes in 4% paraformaldehyde (PFA) dissolved in 10 mM PBS, then placed in 30% sucrose (dissolved in PBS) and stored at 4 °C until cryosectioning. For NMJ staining, the GC muscle was fixed as described above, then placed in 10 mM PBS and stored at 4 °C until the muscle fibre teasing. For proteome profiling and multiplex cytokine immunoassay, the GC, TA and EDL muscles and the spinal cord were removed, homogenised in 10 mM PBS with protease inhibitor (Halt Protease Inhibitor, Cat# 11804111, Thermo Fisher Scientific, Waltham, MA, USA; 1:100 dilution), then 1% Triton X-100 (Cat# X100, Merck Group) was added and the samples were stored at −80 °C until further processing.

## Immunohistochemistry
Patient muscle biopsy samples were embedded in optimal cutting temperature (OCT) compound (Cat# KMA-0100-00A, Cell Path, Newtown, Powys, UK), frozen in nitrogen-cooled isopentane for 1 minute and stored in −80 °C until further use. Muscles were cut in 15 μm-thick transversal sections with a cryostat to allow analysis of muscle fibre architecture. Each slide (J1800AMNZ, Thermo Scientific) contained 3-4 sections from the same muscle and patient. For immunofluorescence staining, samples were cooled down and fixed in 4% PFA 15 min. Samples were permeabilised and blocked in 10% donkey serum in 0.3% Triton X-100 PBS for 1 hour at room temperature. Next, they were incubated with primary antibodies diluted in blocking solution overnight at 4 °C (Supplementary Table 1). On the following day, samples were washed three times in 0.1% Tween-PBS, then incubated with secondary antibodies (Supplementary Table 1) diluted in blocking solution for 1 hour on room temperature. Finally, the samples were washed as described previously and mounted with Fluoromount-G mounting media (Cat# 0100-01, Southern Biotech, Birmingham, AL, USA).

For immune cell labeling on murine samples, muscle samples were embedded in optimal cutting temperature compound, then sectioned longitudinally (30 μm thickness to allow NMJ analysis and compare innervated with non-innervated zones) with a Leica CM1860 cryostat (Leica Biosystems, Wetzlar, Germany), mounted on Superfrost glass slides (Epredia, Portsmouth, NH, USA) and stored at −20 °C

until further processing. For NMJ staining, we carried out muscle fibre teasing, where fibres spanning from the origin to the insertion were dissected. These fibres were then microdissected into small bundles under a dissection microscope, with each bundle consisting of 10-20 individual fibres. To ensure minimal background staining and enhance antibody penetration, any residual fat and connective tissue were removed. These samples were stored in PBS at 4 °C until further use.

Both mounted muscle sections (immune cell labeling) and free-floating sections (NMJ staining) were first rinsed in 10 mM PBS thrice. Free-floating muscle sections were then permeabilized with 10 mM PBS containing 4% Triton X-100 (TPBS) for 60 minutes, followed by two PBS washes. Next, 3% bovine serum albumin (BSA; Cat# 97061-422, VWR International, Radnor, PA, USA) in 0.2% TPBS was applied on both mounted and free-floating samples for 60 min to block nonspecific binding sites. Primary antibodies (Supplementary Table 1) were diluted in the blocking solution and the sections were incubated overnight at 4 °C on an orbital shaker (60 rpm). Next day, sections were washed three times again in PBS, followed by incubation at room temperature in the appropriate secondary antibody (Supplementary Table 1) diluted in blocking solution for 60 min. After washing the samples twice, muscle sections were then incubated for 30 minutes in α-bungarotoxin (BTX, Alexa Fluor 488 conjugate, B13422, Invitrogen, Thermo Fisher Scientific, Waltham, MA, USA), diluted to 1:500 in 10 mM PBS. Finally, sections were thoroughly washed, and 4′,6-diamidino-2-phenylindole (DAPI) (Cat# D3571, Thermo Fisher Scientific) staining was applied where needed, diluted to 1 µg/ml in 10 mM PBS. Free-floating muscle sections were then mounted on single frost glass slides and covered with Fluoromount-G (Cat# 0100–01, Southern Biotech) mounting medium.

## NMJ analysis

NMJ analysis was carried out on fine-dissected GC muscle fibres. The samples were stained with α-BTX and immunohistochemically labeled for SV2A/NEFH, as described previously[30], allowing the visualisation of both the presynaptic and postsynaptic compartments of the NMJs. A minimum of 30 *en-face* NMJs were captured and analysed per muscle sample. Images were captured with Leica SP8 Lightning confocal microscope (Leica Biosystems) on 63x magnification (512×512 pixel frame size, z-stack with 0.5 µm interval). Maximum intensity projection images were used for further analysis. First, NMJs were assessed based on the integrity and occupancy of the pre-synaptic terminal compared to the post-synaptic staining. Based on this, NMJs were characterised as "fully innervated", "partially innervated" or "vacant", as described previously[22]. NMJs were considered to be "partially innervated", when parts of the nerve terminal were clearly absent (more than 20% of the total nerve terminal area), but not to an extent that the NMJ was completely denervated (vacant).

Quantitative analysis of NMJs was carried out with the aNMJ morph macro in FIJI (ImageJ, RRID:SCR_002285, Max Planck Institute of Molecular Cell Biology and Genetics, Dresden, Germany), based on previously published protocols[30].

## Immune cell counting

For the hTDP-43[Tg/Tg] murine experiments, CD45, CD68, and CCR2 cell counting was performed on 30 µm-thick cryosectioned (longitudinal) muscle samples. For CD45 cell counting on patient muscle biopsy samples, quantification was performed on 15 µm-thick cryosectioned (cross-section) samples. CD45 and CD68 staining was used to visualise leukocytes and macrophages, respectively. Additionally, α-BTX staining was used to locate NMJs and DAPI staining to visualise cell nuclei.

For the patient muscle sample quantification, 10 fields of views were captured across the biopsy samples with a Zeiss LSM900 confocal microscope (Carl Zeiss AG) on 20x objective. Each acquired image was composed of 15 optical sections, capturing a comprehensive Z-stack of the muscle structure.

For the CD45 and CD68 counting in the hTDP-43[Tg/Tg] mouse samples, 10-10 fields of views were captured in both the innervation zone (IZ) and in the non-innervation zone (NIZ) with a Leica SP8 Lightning confocal microscope (Leica Biosystems) on 20x magnification (1024 × 1024 pixel frame size, z-stack with 1 µm interval). For CCR2 quantification, the IZ and NIZ were not distinguished; regions of interest were selected randomly within the muscle. The CD45, CD68, and CCR2 cell counting were all based on a modified version of the dissector method and cells were only counted, if the cell nucleus was clearly visible and recognizable.

In the case of CCL2 quantification, 10 IZ images were captured with the same image acquisition settings. Then, the total number of NMJs and the number of NMJs with at least one (perisynaptic) CCL2⁺ cell in the close vicinity of it were quantified and expressed as a ratio. CCL2⁺ cells were considered to be "perisynaptic", if they were either overlapping with the NMJ, or their nucleus was not further than 5 µm from the edge of the endplate.

## Proteome profiler analysis

Mouse XL Cytokine Array Proteome Profiler (Cat# ARY028, R&D Systems) was used for the initial screening of 111 inflammatory proteins. Samples were collected and placed in PBS containing 1% Triton X-100 and protease inhibitor (Halt Protease Inhibitor, Cat# 11804111, Thermo Fisher Scientific; 1:100 dilution), then stored at −80 °C. Before the analysis, samples were homogenised in a Potter–Elvehjem homogeniser with a polytetrafluoroethylene pestle, then centrifuged at 10,000 x g for 5 min to remove debris. Total protein concentrations were quantified by using bicinchoninic acid (BCA) method (Cat# 23225, Thermo Fisher Scientific). Samples from 3 animals (per group) were pooled together and a total 1 mg protein was used for analysis (0.333 mg/animal). The Proteome Profiler array analysis was carried out according to the manufacturer's instructions. The proteome profiler membranes were imaged with a ChemiDoc MP System (RRID:SCR_019037, Bio-Rad, Hercules, CA, USA). Densitometry analysis was performed with the Image Lab Software (version 5.2), by using Proteome Array Analyser plugin (RRID:SCR_014210, Bio-Rad). Data is presented on the heatmap as fold change relative to WT control samples.

## Multiplex chemokine immunoassay

Legendplex technology, a multiplex bead-based immunoassay, was used as described previously with minor modifications[46]. The concentrations of the following 4 proteins were determined: CCL2 (MCP-1), CCL3 (MIP-1α), CCL4 (MIP-1β) and CCL5 (RANTES) of the Mouse Proinflammatory Chemokine Panel (Cat# 740451, Biolegend, San Diego, CA, USA) following the instructions of the manufacturer. Briefly, tissue homogenates (in PBS with 1% Triton X-100 and Halt protease inhibitor) were incubated with the premixed capture beads, and following washing, detection antibodies were added. After washing, streptavidin-PE was finally added. A standard curve was generated by the application of the commercial cytokine standards of the kit. Detection range was 10 ng/ml to 2.44 pg/ml. Samples were acquired on a Cytoflex S FACS (Beckman Coulter, Brea, CA, USA) using the APC and PE channels. Gating strategy is described in Supplementary Fig. 6. Evaluation was performed in CytExpert 4.0 (Beckman Coulter) and Microsoft Excel fitting the median values to the curve of the standards. Data were expressed as the mean of two replicate values in pg/ml, normalized to the protein concentration of each sample.

## Statistical analysis

Statistical analyses were performed using GraphPad Prism (version 8.0.1.244, RRID:SCR_002798, GraphPad Software, San Diego, CA, USA). For each analysis, a Shapiro-Wilk normality test was carried out first, followed by the appropriate statistical test. Results passed the normality test, and therefore, parametric tests were performed, unless

otherwise stated. The specific statistical analysis and n values are indicated in each figure legend. Bars and values represent mean ± standard error of the mean (sem), except stated otherwise.

### Reporting summary

Further information on research design is available in the Nature Portfolio Reporting Summary linked to this article.

## Data availability

The cell counts, raw proteomic data and NMJmorph outputs generated in this study are provided in the Source Data file. Source data are provided with this paper.

## References

1. Masrori, P. & Van Damme, P. Amyotrophic lateral sclerosis: a clinical review. *Eur. J. Neurol.* **27**, 1918–1929 (2020).
2. Baker, M. R. ALS—dying forward, backward or outward?. *Nat. Rev. Neurol.* **10**, 660–660 (2014).
3. Martineau, É, Di Polo, A., Vande Velde, C. & Robitaille, R. Dynamic neuromuscular remodeling precedes motor-unit loss in a mouse model of ALS. *eLife* **7**, e41973 (2018).
4. Tian, F. et al. Monitoring peripheral nerve degeneration in ALS by label-free stimulated Raman scattering imaging. *Nat. Commun.* **7**, 13283 (2016).
5. Fischer, L. R. et al. Amyotrophic lateral sclerosis is a distal axonopathy: evidence in mice and man. *Exp. Neurol.* **185**, 232–240 (2004).
6. Mead, R. J., Shan, N., Reiser, H. J., Marshall, F. & Shaw, P. J. Amyotrophic lateral sclerosis: a neurodegenerative disorder poised for successful therapeutic translation. *Nat. Rev. Drug Discov.* **22**, 185–212 (2023).
7. Zhang, W., Xiao, D., Mao, Q. & Xia, H. Role of neuroinflammation in neurodegeneration development. *Sig Transduct. Target Ther.* **8**, 1–32 (2023).
8. McCombe, P. A., Lee, J. D., Woodruff, T. M. & Henderson, R. D. The peripheral immune system and amyotrophic lateral sclerosis. *Front. Neurol.* **11**, 279 (2020).
9. Béland, L.-C. et al. Immunity in amyotrophic lateral sclerosis: blurred lines between excessive inflammation and inefficient immune responses. *Brain Commun.* **2**, fcaa124 (2020).
10. Baron, P. et al. Production of monocyte chemoattractant protein-1 in amyotrophic lateral sclerosis. *Muscle Nerve* **32**, 541–544 (2005).
11. Tortelli, R. et al. Plasma inflammatory cytokines are elevated in ALS. *Front. Neurol.* **11**, 552295 (2020).
12. Olesen, M. N. et al. Inflammatory profiles relate to survival in subtypes of amyotrophic lateral sclerosis. *Neurology - Neuroimmunology Neuroinflammation* **7**, https://doi.org/10.1212/NXI. 0000000000000697 (2020).
13. Deshmane, S. L., Kremlev, S., Amini, S. & Sawaya, B. E. Monocyte chemoattractant protein-1 (MCP-1): An overview. *J. Interferon Cytokine Res.* **29**, 313–326 (2009).
14. Murdock, B. J. et al. Correlation of peripheral immunity with rapid amyotrophic lateral sclerosis progression. *JAMA Neurol.* **74**, 1446–1454 (2017).
15. Mantovani, S. et al. Immune system alterations in sporadic amyotrophic lateral sclerosis patients suggest an ongoing neuroinflammatory process. *J. Neuroimmunol.* **210**, 73–79 (2009).
16. Beers, D. R. et al. ALS patients' regulatory T lymphocytes are dysfunctional, and correlate with disease progression rate and severity. *JCI Insight* **2**, e89530 (2017).
17. Gustafson, M. P. et al. Comprehensive immune profiling reveals substantial immune system alterations in a subset of patients with amyotrophic lateral sclerosis. *PLOS ONE* **12**, e0182002 (2017).
18. Chen, X. et al. Evidence for peripheral immune activation in amyotrophic lateral sclerosis. *J. Neurological Sci.* **347**, 90–95 (2014).
19. Trias, E. et al. Mast cells and neutrophils mediate peripheral motor pathway degeneration in ALS. *JCI Insight* **3**, e123249 (2018).
20. Van Dyke, J. M. et al. Macrophage-mediated inflammation and glial response in the skeletal muscle of a rat model of familial amyotrophic lateral sclerosis (ALS). *Exp. Neurol.* **277**, 275–282 (2016).
21. Alhindi, A., Boehm, I. & Chaytow, H. Small junction, big problems: Neuromuscular junction pathology in mouse models of amyotrophic lateral sclerosis (ALS). *J. Anat.* **241**, 1089–1107 (2022).
22. Alhindi, A. et al. Neuromuscular junction denervation and terminal Schwann cell loss in the hTDP-43 overexpression mouse model of amyotrophic lateral sclerosis. *Neuropathol. Appl. Neurobiol.* **49**, e12925 (2023).
23. Wegorzewska, I., Bell, S., Cairns, N. J., Miller, T. M. & Baloh, R. H. TDP-43 mutant transgenic mice develop features of ALS and frontotemporal lobar degeneration. *Proc. Natl Acad. Sci.* **106**, 18809–18814 (2009).
24. Gordon, D. et al. Single-copy expression of an amyotrophic lateral sclerosis-linked TDP-43 mutation (M337V) in BAC transgenic mice leads to altered stress granule dynamics and progressive motor dysfunction. *Neurobiol. Dis.* **121**, 148–162 (2019).
25. Tetruashvily, M. M., McDonald, M. A. & Boulanger, L. M. MHCI promotes developmental synapse elimination and aging-related synapse loss at the vertebrate neuromuscular junction. *Brain Behav. Immun.* **56**, 197–208 (2016).
26. Sokol, C. L. & Luster, A. D. The chemokine system in innate immunity. *Cold Spring Harb. Perspect. Biol.* **7**, a016303 (2015).
27. Sewell, W.aC. & Jolles, S. Immunomodulatory action of intravenous immunoglobulin. *Immunology* **107**, 387–393 (2002).
28. Domínguez-Soto, Á. et al. IVIg promote cross-tolerance against inflammatory stimuli in vitro and in vivo. *J. Immunol.* **201**, 41–52 (2018).
29. Yao, M., Smart, C., Hu, Q. & Cheng, N. Continuous delivery of neutralizing antibodies elevate CCL2 levels in mice bearing Mcf10ca1d breast tumor xenografts. *Transl. Oncol.* **10**, 734–743 (2017).
30. Minty, G. et al. aNMJ-morph: a simple macro for rapid analysis of neuromuscular junction morphology. *R. Soc. Open Sci.* **7**, 200128 (2020).
31. Thonhoff, J. R. et al. Combined regulatory T-Lymphocyte and IL-2 treatment is safe, tolerable, and biologically active for 1 year in persons with amyotrophic lateral sclerosis. *Neurol. Neuroimmunol. Neuroinflammation* **9**, e200019 (2022).
32. Ketabforoush, A. H. M. E. et al. Masitinib: The promising actor in the next season of the amyotrophic lateral sclerosis treatment series. *Biomedicine Pharmacother.* **160**, 114378 (2023).
33. Pillon, N. J., Bilan, P. J., Fink, L. N. & Klip, A. Cross-talk between skeletal muscle and immune cells: muscle-derived mediators and metabolic implications. *Am. J. Physiol.-Endocrinol. Metab.* **304**, E453–E465 (2013).
34. Lu, C.-Y. et al. Macrophage-derived vascular endothelial growth factor-A is integral to neuromuscular junction reinnervation after nerve injury. *J. Neurosci.* **40**, 9602–9616 (2020).
35. Chiu, I. M. et al. Activation of innate and humoral immunity in the peripheral nervous system of ALS transgenic mice. *Proc. Natl Acad. Sci.* **106**, 20960–20965 (2009).
36. Orlikowski, D. et al. Monocyte chemoattractant protein 1 and chemokine receptor CCR2 productions in guillain–barré syndrome and experimental autoimmune neuritis. *J. Neuroimmunol.* **134**, 118–127 (2003).

37. Trolese, M. C. et al. Boosting the peripheral immune response in the skeletal muscles improved motor function in ALS transgenic mice. *Mol. Ther.* **30**, 2760–2784 (2022).

38. Blanc, R. S. et al. Inhibition of inflammatory CCR2 signaling promotes aged muscle regeneration and strength recovery after injury. *Nat. Commun.* **11**, 4167 (2020).

39. Arenas, Y. M., Balzano, T., Ivaylova, G., Llansola, M. & Felipo, V. The S1PR2-CCL2-BDNF-TrkB pathway mediates neuroinflammation and motor incoordination in hyperammonaemia. *Neuropathol. Appl. Neurobiol.* **48**, e12799 (2022).

40. Fang, S. et al. CCL2 Knockdown attenuates inflammatory response after spinal cord injury through the PI3K/Akt signaling pathway: Bioinformatics analysis and experimental validation. *Mol. Neurobiol.* **61**, 1433–1447 (2024).

41. Meucci, N. & Nobile-Orazio, E. Intravenous immunoglobulin therapy in amyotrophic lateral sclerosis. *J. Neurol.* **243**, 117–120 (1996).

42. Dalakas, M. C. et al. Effect of high-dose intravenous immunoglobulin on amyotrophic lateral sclerosis and multifocal motor neuropathy. *Arch. Neurol.* **51**, 861–864 (1994).

43. Wils, H. et al. TDP-43 transgenic mice develop spastic paralysis and neuronal inclusions characteristic of ALS and frontotemporal lobar degeneration. *Proc. Natl Acad. Sci.* **107**, 3858–3863 (2010).

44. Perrin, F. E., Lacroix, S., Avilés-Trigueros, M. & David, S. Involvement of monocyte chemoattractant protein-1, macrophage inflammatory protein-1α and interleukin-1β in Wallerian degeneration. *Brain* **128**, 854–866 (2005).

45. Chaytow, H. et al. Targeting phosphoglycerate kinase 1 with terazosin improves motor neuron phenotypes in multiple models of amyotrophic lateral sclerosis. *eBioMedicine* **83**, 104202 (2022).

46. Szabó, E. et al. Identification of immune subsets with distinct lectin binding signatures using multi-parameter flow cytometry: correlations with disease activity in systemic lupus erythematosus. *Front. Immunol.* **15**, 1380481 (2024).

## Acknowledgements

## Author contributions

Conceptualisation: B.N., H.C., T.H.G., Methodology: B.N., K.M., R.K., Y.T.H., Z.R., N.G., A.R., R.P., H.L.S., A.E., S.A.-M., S.F.-A., Investigation: B.N., Z.R., G.J.S., N.G., H.C., I.A.K., A.E., S.A.-M., O.H., S.F.-A., Visualisation: B.N., Z.R., N.G., H.C., Funding acquisition: B.N., R.P., L.S., S.A.-M., H.C., T.H.G., Project administration: B.N., H.C., S.A.-M., T.H.G., Supervision: L.S., P.K., H.C., T.H.G., Writing – original draft: B.N., H.C., Writing – review & editing: B.N., K.M., G.S.Z., L.S., P.K., H.C., T.H.G.

## Competing interests

T.H.G. has provided advisory services for Roche and Novartis. S.A.-M. is a named inventor on a patent related to neurological disorders (PCT/EP2021/064274 and US 2024/0277695 A1), entitled "FOXO inhibitors for use in the treatment of diseases caused by abnormal processing of TDP-43 and/or FUS proteins", not related to this study. SA-M also has ownership in Miaker Developments S.L., a startup related with a pipeline on Neurodegenerative and Neuromuscular Diseases. There are no other competing interests.

## Additional information